J. Fluid Mech. (2019), *vol.* 874, *pp.* 573–605. © Cambridge University Press 2019
doi:10.1017/jfm.2019.464

Stability of Poiseuille flow of a Bingham fluid overlying an anisotropic and inhomogeneous porous layer

Sourav Sengupta[1] **and Sirshendu De**[1,†]

[1]Department of Chemical Engineering, Indian Institute of Technology Kharagpur, Kharagpur 721302, India

(Received 1 September 2018; revised 30 May 2019; accepted 5 June 2019; first published online 11 July 2019)

Modal and non-modal stability analyses are performed for Poiseuille flow of a Bingham fluid overlying an anisotropic and inhomogeneous porous layer saturated with the same fluid. In the case of modal analysis, the resultant Orr–Sommerfeld type eigenvalue problem is formulated and solved via the Chebyshev collocation method, using QZ decomposition. It is found that no unstable eigenvalues are present for the problem, indicating that the flow is linearly stable. Therefore, non-modal analysis is attempted in order to observe the short-time response. For non-modal analysis, the initial value problem is solved, and the response of the system to initial conditions is assessed. The aim is to evaluate the effects on the flow stability of porous layer parameters in terms of depth ratio (ratio of the fluid layer thickness d to the porous layer thickness d_m), Bingham number, Darcy number and slip coefficient. The effects of anisotropy and inhomogeneity of the porous layer on flow transition are also investigated. In addition, the shapes of the optimal perturbations are constructed. The mechanism of transient growth is explored to comprehend the complex interplay of various factors that lead to intermediate amplifications. The present analysis is perhaps the first attempt at analysing flow stability of viscoplastic fluids over a porous medium, and would possibly lead to better and efficient designing of flow environments involving such flow.

Key words: instability control, porous media, transition to turbulence

1. Introduction

Viscoplastic fluids constitute a special class of non-Newtonian fluids. They are uniquely characterized by exhibition of a threshold shear stress (known as yield stress), below which they do not undergo deformation and show ideal rigid-solid behaviour. When the shear stress is more than the yield stress, the fluid behaves as viscous (Bird, Dai & Yarusso 1983). Such fluids find applications in varied fields such as food and dairy processing, oil exploration, biological fluids, etc. (Chhabra & Richardson 1999; Balmforth, Frigaard & Ovarlez 2014; Tripathi *et al.* 2018). Viscoplastic behaviour is exhibited by colloidal gels, emulsions, slurries, suspensions, nanocomposites,

†Email address for correspondence: sde@che.iitkgp.ac.in

drilling muds, cement, etc. Stability analysis of fluid flow is essential to determine the physical scenario under which there is departure from laminar behaviour, so that it can be either avoided or exploited for potential enhancement in heat and mass transfer. One of the earliest attempts at stability analysis of Poiseuille flow of viscoplastic fluids was made by Pavlov, Romanov & Simkhovich (1974). By means of changing the scale of the characteristic length and velocity parameters, the problem was reduced to Couette–Poiseuille flow of a Newtonian fluid, and thus inferred to be stable for infinitesimal disturbances. Pavlov, Romanov & Simkhovich (1975) further extended the work to consider the scenario of finite-amplitude disturbances to explain the experimental findings on transition to turbulence of viscoplastic fluids. One of the major limitations of Pavlov *et al.* was that they considered the analogous Newtonian stability problem, without commenting on three-dimensional perturbations. In the case of Newtonian fluids, Squire's theorem asserts that a two-dimensional perturbation is able to make a flow unstable at lower Reynolds number, compared to three-dimensional perturbations (Squire 1933; Drazin & Reiid 2004). However, Squire's theorem is not applicable for Bingham (viscoplastic) fluids, as rightly pointed out by subsequent researchers (Frigaard, Howison & Sobey 1994; Nouar & Frigaard 2001; Nouar *et al.* 2007; Métivier & Nouar 2011). A comprehensive modal linear stability analysis (incorporating perturbation in the yield surface) of Poiseuille flow of a Bingham fluid was undertaken by Frigaard *et al.* (1994). The study revealed that the system is unconditionally linearly stable for a one-dimensional perturbation.

Linear stability analysis of two-layer channel flow involving viscoplastic fluids was also undertaken, and it was shown that multilayer flow comprising two Bingham fluids is more stable than the equivalent flow of either fluid alone (Pinarbasi & Liakopoulos 1995; Frigaard 2001). Pinarbasi & Liakopoulos (1995) performed the analysis systematically by first starting with a two-layer Newtonian fluid flow, and showed that replacing the Newtonian fluid with a Bingham fluid at the bottom layer stabilizes the interface between the two fluids. Having two Bingham fluids stabilized the flow even further, with an increase in yield stress favouring stability. They concluded the study by analysing the behaviour of two shear-thinning fluids, and demonstrated that an increase in shear thinning leads to flow destabilization. Linear stability analysis of two-layer channel flow consisting of a viscoplastic fluid and a Newtonian fluid subject to two- and three-dimensional perturbations was undertaken by Sahu *et al.* (2007) and Sahu & Matar (2010). However, there is a major difference in the assumptions of the analyses performed by Frigaard (2001) and Sahu *et al.* (2007). In the case of viscoplastic fluids, yield stress is known to influence the growth of waves at the interface, consequently affecting the rate of removal of the highly viscous layer. The study by Frigaard (2001) considered the presence of a plug zone in between the Newtonian fluid and the unyielded zone of the Bingham fluid. As a result, the interfacial modes were suppressed in their study, resulting in super-stable two-layer flows similar to pressure-driven single-fluid flow. Sahu *et al.* (2007) removed this interfacial plug zone in their analysis. Owing to this, the interfacial modes no longer remained suppressed. This resulted in an interesting observation: enhancement of dimensionless yield stress (quantified by Bingham number) prior to the development of a plug zone had a destabilizing effect. Nouar & Frigaard (2001) carried out a nonlinear energy stability analysis of the Poiseuille flow of a Bingham fluid, and observed that the critical energy Reynolds number increases as $Bn^{0.5}$ for large values of Bn, Bn being the Bingham number (the ratio of the yield stress to the viscous stress of the fluid). In their analysis, the yield stress of the fluid did not directly contribute to the viscous dissipation. Instead, the effect of yield stress

was implicitly present in the Reynolds number through the modification of the yielded zone width, and also through the gradient of the base velocity profile. Frigaard & Nouar (2003) analysed the linear stability of the Poiseuille flow of a Bingham fluid to three-dimensional disturbances, and determined the eigenvalue bounds. For large Bn, they observed the variation of critical Reynolds number as $Bn^{0.75}$. However, they did not consider the limiting case of Bn close to zero. Nevertheless, the limiting problem was attempted by Métivier, Nouar & Brancher (2005). In comparison with a Newtonian fluid, they observed a discontinuity of the critical conditions. Thus, the critical conditions for $Bn \to 0$ are different compared to a Newtonian fluid ($Bn = 0$). This discontinuity arises because of the assumption of a plug zone. They opined that the replacement of the plug zone by assuming a suitable biviscous model could possibly eradicate the discontinuity.

Non-modal stability analyses for plane Poiseuille as well as Hagen–Poiseuille flow of viscoplastic fluids (Bingham and Herschel–Bulkley) have also been performed (Nouar *et al.* 2007; Liu & Liu 2014; Bentrad *et al.* 2017; Liu, Ding & Hu 2018). The study by Nouar *et al.* (2007) involved demonstration of the shape of optimal perturbation, and its variation with dimensionless yield stress. The reduction in the transient energy growth observed in their study, compared to plane Poiseuille flow of a Newtonian fluid, may be attributed to increase in the viscous dissipation caused by the viscoplastic behaviour of the fluid. The stability of Rayleigh–Bénard–Poiseuille (RBP) flow for viscoplastic fluids was studied, both with and without the assumption of thermal dependence, as well as by considering the effect of wall slip (Métivier & Nouar 2008, 2009, 2011; Métivier, Frigaard & Nouar 2009; Métivier, Nouar & Brancher 2010; Métivier & Magnin 2011). The stabilizing effect of Bn in these studies is possibly because of the vanishing of velocity perturbations at the yield surface for smaller values of Bn, and augmentation in effective viscous dissipation at higher values of Bn. Nouar & Bottaro (2010) studied the stability of a Bingham fluid in a channel with emphasis on eigenvalue sensitivity analysis. They observed that very weak defects can successfully excite exponentially amplified streamwise travelling waves. However, they neglected a fundamental fact that the stability operator encountered in shear planar flow of the fluid is non-normal in nature. Thus, ignoring the interplay between transient amplifications and exponential growth was a major limitation in their analysis. Moyers-Gonzalez, Burghelea & Mak (2011) performed linear stability analysis for plane Poiseuille flow of an elastoviscoplastic fluid, a marked departure from the traditional consideration of a viscoplastic fluid. Instead of assuming a direct solid–fluid transition regime, they considered a solid–fluid coexistence regime where the behaviour of the material is viscoelastic. The findings of their study resemble those of a normal viscoplastic fluid, possibly because the viscoelastic core is limited to a region away from the wall boundary. In addition to flow in parallel channels, the stability of viscoplastic fluids has also been analysed for an annular geometry (Kabouya & Nouar 2003; Moyers-Gonzalez, Frigaard & Nouar 2004; Peng & Zhu 2004; Caton 2006; Landry, Frigaard & Martinez 2006; Soleimani & Sadeghy 2010, 2011; Madani *et al.* 2013).

As stated in the beginning, viscoplastic fluids assume importance due to their widespread presence in various physically relevant systems (e.g. blood flow, drilling mud, toothpaste). An understanding of the conditions under which flow transition occurs in viscoplastic fluids may possibly lead to better design of flow equipment involving the flow of such fluids. Stability studies on a Bingham fluid in a non-porous channel show that the critical Reynolds number increases with the Bingham number of the fluid (Frigaard *et al.* 1994; Balmforth *et al.* 2014). Thus, yield stress adds to

the stability of the flow in general for non-porous channels. Actually, the plug region of the Bingham flow helps in resisting transition even when finite perturbations are introduced in the channel. But stability analysis of the flow of viscoplastic fluids over a porous layer has remained unexplored till now. However, several real-life applications, like oil recovery, biological transport, deep filtration, etc., involve the flow of viscoplastic fluids over porous media (Herzig, Leclerc & Goff 1970; Dash, Mehta & Jayaraman 1996; Mandal & Bera 2015). Hence, stability analysis of viscoplastic fluid flow over a porous media is of considerable interest. Although studies exploring the analytical solutions for the flow of Bingham fluids involving a porous interface exist (Chen & Zhu 2008; Sengupta & De 2019), there has been no stability analysis on the same. This lack of literature on the stability analysis of viscoplastic fluids involving porous media has necessitated the current study. Linear stability analysis is important, as it provides an upper limit on the critical Reynolds number necessary for flow to become unstable, leading to undesirable flow manifestations, like unwanted mixing. In addition, it provides useful insight into the role played by yield stress in viscoplastic fluids. The Bingham model, while providing a simplistic representation of viscoplastic fluids, also incorporates the essential element of viscoplastic behaviour, i.e. yield stress, thereby making the analysis intriguing.

To the best of the authors' knowledge, there are no reported studies on the stability analysis of Bingham fluids over a porous layer for any kind of flow configuration. In addition, non-modal stability analysis for flow over porous media is rare. For analysing fluid flow over a porous layer, earlier studies have adopted modal analysis (Chang, Chen & Straughan 2006; Hill & Straughan 2008, 2009; Deepu, Anand & Basu 2015; Chang, Chen & Chang 2017). A literature review suggests that variation in porous layer parameters, like permeability, depth ratio, slip parameter, etc., can induce instability via the fluid–porous interface in the case of Newtonian fluids (Chang *et al.* 2006; Hill & Straughan 2008; Chang *et al.* 2017). Linear stability analysis shows that the critical Reynolds number for porous configuration (Re_{cr}) can be as low as approximately 2500, which is significantly lower than that of non-porous configuration ($Re_{cr} = 5772$) (Chang *et al.* 2006). In fact, in the case of a fluid–porous system, there is a rapid change in velocity at the interface, which is difficult to avoid. This velocity gradient at the interface is known to influence the flow transition characteristics significantly. Thus, the authors are interested in exploring how the presence of a porous layer affects the flow transition in the case of Bingham fluids. This was the major motivation behind attempting the current study.

Bingham flows are obviously known to be more stable. Thus, the current study aims to investigate whether the presence of the porous layer is able to impact this stable flow. Since the modal analysis underpredicts the experimentally observed critical point in many cases, a non-modal analysis is attempted (because, for example, modal analysis predicts $Re_{cr} = 5772$ for plane Poiseuille flow of Newtonian fluids, while it is around 2000 in real experimental observations). Moreover, a literature review reveals that non-modal studies on Bingham fluids in non-porous channels have shown the presence of a transient growth that decays at large time (Nouar *et al.* 2007). Thus, there is substantial evidence that non-modal studies give insight into the transient amplifications for Newtonian as well as non-Newtonian fluids. However, to the best of our knowledge, non-modal analysis in a fluid–porous system is rare in the open literature. Moreover, in a practical scenario, a porous layer has a high possibility to exhibit directional variations in the permeability (Straughan & Walker 1996; Malashetty & Mahantesh 2010). Thus, it is imperative to consider anisotropy and inhomogeneity of the porous layer, and analyse its effects on the flow stability for an exhaustive understanding of practical applications involving fluid–porous systems.

In the modal analysis, asymptotic long-time stability behaviour is analysed. However, the response to infinitesimal perturbations at short times has not been explored for a porous configuration. This necessitates the analysis of the response to external excitations and initial conditions, in order to gain a more holistic understanding of the fluid flow transition. In terms of non-modal analysis, the resolvent and the growth functions give an indication about the amplification of the external excitations and the initial conditions. The importance of non-modal analysis can be stressed by the fact that there is always a possibility for occurrence of subcritical transition if a non-normal linear stability operator is present, as in shear flows (Schmid & Henningson 1992; Henningson, Lundbladh & Johansson 1993; Reddy & Henningson 1993). Mathematically, it implies that there is a possibility for energy extraction from the basic flow by a perturbation subspace. This may lead to a transient growth, even though there is no long-time instability.

In the current work, an attempt has been made to carry out temporal linear stability analysis of Poiseuille flow of a Bingham fluid overlying an anisotropic and inhomogeneous porous layer. The constitutive equation for a Bingham fluid has been considered together with the governing conservation equations, and the base velocity profile is derived for the chosen flow configuration. Thereafter, an Orr–Sommerfeld equation-like framework is obtained. Since traditional eigenvalue analysis did not yield any unstable eigenvalue, non-modal analysis has also been attempted. The effect of the porous layer parameters on the stability behaviour has been identified in terms of transient growth curves. Critical energy Reynolds-number curves are also obtained in order to comprehend the kinetic energy of the perturbations. To gain insight regarding the short-time behaviour, the initial growth rate and pseudospectra curves are also constructed. The authors believe that the present study provides a much-needed framework for a basic understanding of the stability of viscoplastic fluids over a porous layer. The current study is envisaged to be of critical help in the better design of equipment dealing with Bingham-type flow, as observed in the case of drilling mud, nanocomposites, etc. As already emphasized, studies involving non-modal stability analysis for flow over porous media are rare for non-Newtonian fluids. The current work aims to bridge this gap.

2. Problem formulation

The geometry of the flow configuration is elucidated in figure 1. A Bingham fluid of density ρ flows in a channel overlying a porous medium having thickness d_m. There are two distinct flow regions: an unobstructed layer of fluid where no porous medium is present, and a porous layer beneath it, where the fluid flows through the porous medium in the axial direction, i.e. in the same direction as that of the unobstructed zone. The thickness of the unobstructed zone (also referred to hereafter as the fluid layer, being the zone where no porous medium is present) is d (extending from $z=0$ to d). The porous medium is of thickness d_m. The porous layer is saturated with the same fluid. The bottom of the porous layer is impermeable, i.e. at $z=-d_m$, $w_m=0$, where w_m refers to the normal velocity component in the porous layer. The flow occurs under the action of an applied constant pressure gradient $(-\mathrm{d}p/\mathrm{d}x)$ in the x direction. The yield surfaces are located at $z=z_{01}$ and z_{02}. It may be noted that the velocity profile is expected to be asymmetric with respect to the centreline of the channel $(z=d/2)$, due to the presence of the porous layer. This is evident from the schematic given in figure 1.

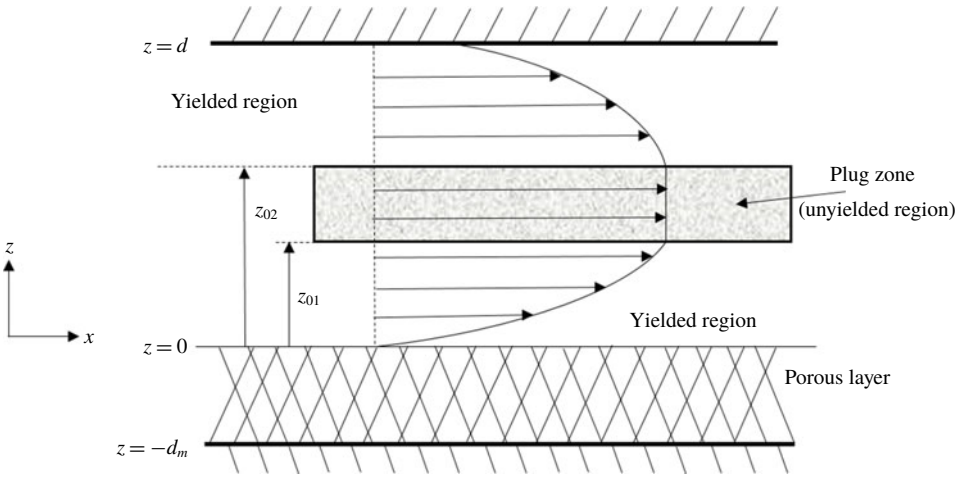

FIGURE 1. Flow configuration for plane Poiseuille flow of a Bingham fluid overlying a porous layer.

2.1. *Governing equations*

Now, the mass conservation equation and Cauchy's momentum equation in the fluid layer are given as

$$\left.\begin{aligned} \boldsymbol{\nabla}\cdot\boldsymbol{u} &= 0, \\ \rho\frac{\mathrm{D}\boldsymbol{u}}{\mathrm{D}t} &= -\boldsymbol{\nabla}p + \boldsymbol{\nabla}\cdot\boldsymbol{\tau}. \end{aligned}\right\} \tag{2.1}$$

Equation (2.1) is simplified to obtain the x-momentum equation as

$$0 = -\left(\frac{\mathrm{d}p}{\mathrm{d}x}\right) + \frac{\mathrm{d}\tau}{\mathrm{d}z}. \tag{2.2}$$

In the above equation, τ is the shear stress of the fluid.

The constitutive relation for a Bingham fluid is expressed as

$$\left.\begin{aligned} \tau &= \mu\frac{\mathrm{d}u}{\mathrm{d}z} + \tau_0\,\mathrm{sgn}\left(\frac{\mathrm{d}u}{\mathrm{d}z}\right), && |\tau| \geqslant \tau_0, \\ \frac{\mathrm{d}u}{\mathrm{d}z} &= 0, && |\tau| < \tau_0, \end{aligned}\right\} \tag{2.3}$$

where $u = u(z)$ is the streamwise velocity component, τ_0 and μ represent the yield stress and the plastic viscosity of the Bingham fluid, and sgn denotes the signum function.

For characterizing flow in the anisotropic porous medium, the governing equations are

$$\left.\begin{aligned} \boldsymbol{\nabla}\cdot\boldsymbol{u}_m &= 0, \\ \left(\frac{\rho}{\chi}\right)\frac{\partial\boldsymbol{u}_m}{\partial t} &= -\boldsymbol{\nabla}p_m - \frac{\mu}{\boldsymbol{K}}\boldsymbol{u}_m. \end{aligned}\right\} \tag{2.4}$$

In the above equation, $\boldsymbol{u}_m$ is the velocity vector in the porous layer, and p_m is the interstitial pressure. Also, χ is the porosity, and $\boldsymbol{K}$ is a diagonal tensor used to

represent the anisotropic and inhomogeneous permeability of the porous medium. This tensor is expressed as $\boldsymbol{K} = K_x\eta_x(z/d_m)\boldsymbol{ii} + K_y\eta_y(z/d_m)\boldsymbol{jj} + K_z\eta_z(z/d_m)\boldsymbol{kk}$, where $\boldsymbol{i}$, $\boldsymbol{j}$ and $\boldsymbol{k}$ are the unit vectors in the x, y and z directions, respectively. In this expression, K_x, K_y and K_z represent the permeabilities in the x, y and z directions; and η_x, η_y and η_z denote the respective inhomogeneity functions. A generalized formulation would allow each of these inhomogeneity functions to be multivariate. However, in the present study, η_x, η_y and η_z have been assumed to be functions of z only. This is done in order to ensure that the base solution is not multidimensional in nature. In this study, an exponential variation of the inhomogeneity function is assumed, $\eta_x = \eta_y = \eta_z = \exp(A_{inh}(1+\bar{z}_m))$, where A_{inh} is the inhomogeneity factor (Chen & Hsu 1991), and $\bar{z}_m$ is the dimensionless distance in the porous layer (as defined later in (2.10)). Continuity of pressure is assumed at the fluid–porous interface, i.e. $p = p_m$ (Beavers & Joseph 1967).

The velocity profile in the porous layer is given by the plane Buckingham–Reiner model (Rees 2015). In the present notation of variables, it is expressed as

$$u_m = -\frac{K_x\eta_x}{\mu}\left[1 - \frac{3}{2}\left(\frac{\alpha_0}{\left|\dfrac{\mathrm{d}p}{\mathrm{d}x}\right|}\right) + \frac{1}{2}\left(\frac{\alpha_0}{\left|\dfrac{\mathrm{d}p}{\mathrm{d}x}\right|}\right)^3\right]\left(\frac{\mathrm{d}p}{\mathrm{d}x}\right), \quad \text{for} \quad \left|\frac{\mathrm{d}p}{\mathrm{d}x}\right| > \alpha_0, \tag{2.5}$$

where $\alpha_0 = (\beta_0\tau_0)/\sqrt{K_x}$ is essentially the threshold gradient, i.e. the limiting pressure gradient for flow to occur, and β_0 is a dimensionless parameter. When the applied pressure gradient is unable to exceed the threshold gradient, there is no flow in the porous layer. It may be observed that the velocity in the porous layer continuously approaches zero, as the limiting pressure gradient is attained. This is a characteristic feature of Bingham flow in porous media, as also confirmed by pore-scale studies (Balhoff & Thompson 2004; Nash & Rees 2017).

The authors recognize the prevalence of the Darcy–Brinkman model for describing porous layer flow. Brinkman (1949) suggested the incorporation of a viscous stress component in the Darcy equation. The study describes an 'effective viscosity' to be used in the viscous stress term. However, it seems that there is a lack of consensus in the literature regarding the definition of this effective viscosity (Liu & Liu 2009). In addition, it appears that most researchers have agreed upon the fact that the Brinkman model is applicable for high-porosity configurations (Nield & Bejan 2006; Auriault 2009). A detailed Stokesian dynamics study for flow in porous media was carried out by Durlofsky & Brady (1987), and they concluded that Brinkman's equation should be used for porosity greater than 0.95. On the contrary, in our analysis, we considered a porosity of only 0.1, for which the validity of the Brinkman model is undoubtedly debatable. Typical application of a viscoplastic fluid flow over a porous layer is in oil recovery, where drilling fluid flows over porous soil. The porosity of major varieties of soil lies in the range of 0.1–0.4 (Association of Swiss Road and Traffic Engineers 1999; Das 2013). Other researchers who have considered the porosity in a similar range (0.1–0.4) have also neglected the Brinkman model for the similar reason of a low-porosity configuration (Chang *et al.* 2006; Deepu *et al.* 2015, 2016; Chang *et al.* 2017). Only researchers who have carried out the analysis for a 'highly porous material' have adopted the Brinkman model (Hill & Straughan 2008, 2009). These are the major factors why the Brinkman model is not considered to describe the flow in porous medium in this study. Incorporation of the Brinkman model can be suitably done in a future study, exploring the stability of a flow configuration consisting of a highly porous medium.

2.2. *Boundary conditions*

At the upper wall, the no-slip boundary condition is assumed, i.e.

$$\text{at } z = d, \quad u = 0. \tag{2.6a,b}$$

The fluid–porous interface ($z = 0$) is described by the Beavers–Joseph boundary condition (Beavers & Joseph 1967), i.e.

$$\text{at } z = 0, \quad \frac{\mathrm{d}u}{\mathrm{d}z} = \frac{\alpha_{BJ}}{\sqrt{K_x \eta_x(0)}}(u - u_m), \tag{2.7a,b}$$

where α_{BJ} is the Beavers–Joseph constant. For a Bingham fluid, the velocity remains invariant within the plug zone. In addition, both the velocity and its gradient are assumed to be continuous at both yield surfaces. Therefore,

$$u|_{z=z_{01}} = u|_{z=z_{02}}, \tag{2.8}$$

and

$$\left.\frac{\mathrm{d}u}{\mathrm{d}z}\right|_{z=z_{01}} = \left.\frac{\mathrm{d}u}{\mathrm{d}z}\right|_{z=z_{02}} = 0. \tag{2.9}$$

2.3. *Non-dimensionalization*

The variables are made non-dimensional as follows:

$$\bar{z} = \frac{z}{d}, \quad \bar{z}_m = \frac{z}{d_m}, \quad \bar{u} = \frac{u}{U_p}, \quad \bar{\tau} = \frac{\tau d}{\mu U_p}, \tag{2.10a–d}$$

where $U_p = (d^2/\mu)(-\mathrm{d}p/\mathrm{d}x)$.

2.3.1. *Non-dimensional governing equations*

Equation (2.2) may be represented in terms of non-dimensional variables as

$$1 + \frac{\mathrm{d}\bar{\tau}}{\mathrm{d}\bar{z}} = 0, \tag{2.11a}$$

i.e.

$$\bar{\tau} = -\bar{z} + l_1, \tag{2.11b}$$

where l_1 is the integration constant.

The constitutive relation for a Bingham fluid (2.3) may be represented in dimensionless form as

$$\left.\begin{aligned} \bar{\tau} &= \frac{\mathrm{d}\bar{u}}{\mathrm{d}\bar{z}} + Bn\,\mathrm{sgn}\left(\frac{\mathrm{d}\bar{u}}{\mathrm{d}\bar{z}}\right), && |\bar{\tau}| \geqslant Bn, \\ \frac{\mathrm{d}\bar{u}}{\mathrm{d}\bar{z}} &= 0, && |\bar{\tau}| < Bn. \end{aligned}\right\} \tag{2.12}$$

In the above equation, $Bn = (\tau_0 d)/(\mu U_p)$ is the Bingham number of the fluid.

2.3.2. *Non-dimensional boundary conditions*

The boundary conditions (2.6)–(2.9) may be recast in terms of dimensionless variables:

$$\text{at } \bar{z}=1, \quad \bar{u}=0, \tag{2.13a,b}$$

$$\text{at } \bar{z}=0, \quad \frac{\mathrm{d}\bar{u}}{\mathrm{d}\bar{z}}=\frac{\alpha_{BJ}\hat{d}}{\delta\sqrt{\eta_x(0)}}(\bar{u}-\bar{u}_m), \tag{2.14a,b}$$

$$\bar{u}|_{\bar{z}=\bar{z}_{01}}=\bar{u}|_{\bar{z}=\bar{z}_{02}}, \tag{2.15}$$

$$\left.\frac{\mathrm{d}\bar{u}}{\mathrm{d}\bar{z}}\right|_{\bar{z}=\bar{z}_{01}}=\left.\frac{\mathrm{d}\bar{u}}{\mathrm{d}\bar{z}}\right|_{\bar{z}=\bar{z}_{02}}=0, \tag{2.16}$$

where $\delta=\sqrt{K_x}/d_m$ represents the Darcy number, and $\hat{d}=d/d_m$ is the ratio of the thicknesses of the fluid and the porous layers; $\hat{d}$ is referred to as the depth ratio of the channel.

2.4. *Base flow – analytical solution*

The velocity profile may be derived by solving (2.11) subject to boundary conditions (2.13)–(2.16). For the region $0\leqslant\bar{z}\leqslant\bar{z}_{01}$ (i.e. the lower shear zone), $\mathrm{d}\bar{u}/\mathrm{d}\bar{z}>0$, i.e. the velocity gradient is positive. The velocity may be given as

$$\bar{u}=\left(l_1\bar{z}-\frac{\bar{z}^2}{2}-Bn\,\bar{z}\right)+l_2. \tag{2.17a}$$

In the upper shear zone (i.e. $\bar{z}_{02}\leqslant\bar{z}\leqslant 1$), $\mathrm{d}\bar{u}/\mathrm{d}\bar{z}<0$. The velocity is expressed as

$$\bar{u}=\left(l_1\bar{z}-\frac{\bar{z}^2}{2}+Bn\,\bar{z}\right)+l_3, \tag{2.17b}$$

where l_2 and l_3 are the integration constants.

For the intermediate unyielded zone ($\bar{z}_{01}\leqslant\bar{z}\leqslant\bar{z}_{02}$), the velocity is constant, given by $\bar{u}|_{\bar{z}=\bar{z}_{01}}=\bar{u}|_{\bar{z}=\bar{z}_{02}}$.

2.4.1. *Velocity profile in the fluid layer*

The dimensionless base velocity in the fluid layer may be given as ($\bar{v}$ and $\bar{w}$ represent the dimensionless spanwise and normal velocity components)

$$\left.\begin{aligned}\bar{u}(\bar{z})&=\left(l_1\bar{z}-\frac{\bar{z}^2}{2}-Bn\,\bar{z}\right)+l_2, \quad 0\leqslant\bar{z}\leqslant\bar{z}_{01},\\ &=\frac{\bar{z}_{01}^2}{2}+l_2, \quad \bar{z}_{01}\leqslant\bar{z}\leqslant\bar{z}_{02},\\ &=\left(l_1\bar{z}-\frac{\bar{z}^2}{2}+Bn\,\bar{z}\right)+l_3, \quad \bar{z}_{02}\leqslant\bar{z}\leqslant 1,\\ \bar{v}&=0, \quad \bar{w}=0, \quad 0\leqslant\bar{z}\leqslant 1,\end{aligned}\right\} \tag{2.18}$$

where

$$l_1=Bn+\frac{\alpha_{BJ}\hat{d}}{\delta\sqrt{\eta_x(0)}}[l_2-\bar{u}_m(0)], \tag{2.19}$$

$$l_2 = \left[\frac{1 - 4Bn(1-Bn) + \dfrac{2\bar{u}_m(0)\alpha_{BJ}\hat{d}(1-2Bn)}{\delta\sqrt{\eta_x(0)}}}{2\left(1 + \dfrac{\alpha_{BJ}\hat{d}(1-2Bn)}{\delta\sqrt{\eta_x(0)}}\right)} \right], \tag{2.20}$$

$$l_3 = \frac{1}{2} - 2Bn - \frac{\alpha_{BJ}\hat{d}}{\delta\sqrt{\eta_x(0)}}[l_2 - \bar{u}_m(0)]. \tag{2.21}$$

The locations of the yield surfaces at $\bar{z}_{01}$ and $\bar{z}_{02}$ are expressed as

$$\bar{z}_{01} = \frac{\alpha_{BJ}\hat{d}}{\delta\sqrt{\eta_x(0)}}[l_2 - \bar{u}_m(0)], \tag{2.22}$$

$$\bar{z}_{02} = 2Bn + \frac{\alpha_{BJ}\hat{d}}{\delta\sqrt{\eta_x(0)}}[l_2 - \bar{u}_m(0)]. \tag{2.23}$$

Using (2.22) and (2.23), it is observed that

$$\bar{z}_{02} = 2Bn + \bar{z}_{01}. \tag{2.24}$$

It is evident that the plug region should be within the fluid volume. Therefore, the following constraint is imposed on $\bar{z}_{01}$ and $\bar{z}_{02}$:

$$0 < \bar{z}_{01} < 1, \quad 0 < \bar{z}_{02} < 1. \tag{2.25a,b}$$

In addition, it may be inferred from (2.24) and (2.25) that

$$Bn < 0.5. \tag{2.26}$$

2.4.2. *Velocity profile in the porous layer*

The non-dimensional velocity profile in the porous layer is obtained as

$$\left.\begin{array}{llll} \bar{u}_m(\bar{z}_m) = l_4\eta_x(\bar{z}_m), & -1 \leqslant \bar{z}_m \leqslant 0, \\ \bar{v}_m = 0, \quad \bar{w}_m = 0, & -1 \leqslant \bar{z}_m \leqslant 0, \end{array}\right\}, \quad \text{for } \frac{\delta}{\beta_0\hat{d}} > Bn, \tag{2.27}$$

where

$$l_4 = \frac{\delta^2}{\hat{d}^2}\left[1 - \frac{3}{2}\left(\frac{\beta_0 Bn\,\hat{d}}{\delta}\right) + \frac{1}{2}\left(\frac{\beta_0 Bn\,\hat{d}}{\delta}\right)^3\right]. \tag{2.28}$$

When the threshold gradient is not reached (i.e. when $\delta/\beta_0\hat{d} < Bn$), the velocity is zero in the porous layer.

2.5. *Stability analysis*

In earlier studies on stability analysis of viscoplastic fluids, there was no existence of the porous layer. As a result, the flow profile was symmetric about the middle of the plug zone. This eliminated the need to consider both the shear zones in the analysis. Stability analysis for the decoupled problem was carried out only for the upper shear zone. Here, it may be noted that the flow configuration consists of an upper shear zone, a plug zone, a lower shear zone and a porous layer. The complexity

of the current study is enhanced by the fact that the velocity profile is asymmetric about the middle of the plug zone. There are two flow domains, separated by a plug zone discontinuity. One is the domain I comprising the porous layer and the lower shear zone, extending from $z=-d_m$ to z_{01}. The other is the domain II, consisting of the upper shear zone, extending from $z=z_{02}$ to d. Fortunately, it may be noted that the maximum velocity is the same for both domains, and is realized at the interface of the shear and plug zones. It is evident that the governing perturbation equations will be the same for both the shear zones. Since the maximum realizable velocity is the same in either of the two shear zones, for the current study, we carry out the stability analysis for the domain I. In other words, we study the zone extending from $z=-d_m$ to z_{01} (comprising the porous layer and the lower shear zone). Henceforth, z_{01} is represented as z_0 for the sake of simplicity.

2.5.1. *Perturbation equations*

Now, we allow a perturbation to the system in the form

$$\left.\begin{array}{c} u=\overline{u}+u', \quad v=\overline{v}+v', \quad w=\overline{w}+w', \\ u_m=\overline{u_m}+u'_m, \quad v_m=\overline{v_m}+v'_m, \quad w_m=\overline{w_m}+w'_m, \\ p=\overline{p}+p', \quad z_0=\overline{z_0}+h', \end{array}\right\} \tag{2.29}$$

where $\bar{u}$ and u' respectively denote x-direction steady-state velocity, and the velocity perturbation. The rest of the variables also have analogous meanings.

The perturbation equations for the fluid layer are given as ($\mathrm{D}=\mathrm{d}/\mathrm{d}z$; in addition, we write $\bar{u}=U$ for convenience in the following equations)

$$\frac{\partial u'}{\partial x}+\frac{\partial v'}{\partial y}+\frac{\partial w'}{\partial z}=0, \tag{2.30}$$

$$\begin{aligned}\frac{\partial u'}{\partial t}+U\frac{\partial u'}{\partial x}+w'\mathrm{D}U \;=\; & -\frac{\partial p'}{\partial x}+\frac{1}{Re}\nabla^2 u' \\ & +\frac{Bn}{Re}\frac{1}{|\mathrm{D}U|}\left(\nabla^2 u'-\frac{\partial^2 w'}{\partial x\partial z}-\frac{\partial^2 u'}{\partial z^2}\right),\end{aligned} \tag{2.31}$$

$$\begin{aligned}\frac{\partial v'}{\partial t}+U\frac{\partial v'}{\partial x} \;=\; & -\frac{\partial p'}{\partial y}+\frac{1}{Re}\nabla^2 v' \\ & +\frac{Bn}{Re}\left[\frac{\nabla^2 v'}{|\mathrm{D}U|}+\left(\frac{\partial v'}{\partial z}+\frac{\partial w'}{\partial y}\right)\left\{\frac{\mathrm{d}}{\mathrm{d}z}\left(\frac{1}{|\mathrm{D}U|}\right)\right\}\right],\end{aligned} \tag{2.32}$$

$$\begin{aligned}\frac{\partial w'}{\partial t}+U\frac{\partial w'}{\partial x} \;=\; & -\frac{\partial p'}{\partial z}+\frac{1}{Re}\nabla^2 w' \\ & +\frac{Bn}{Re}\left[2\left(\frac{\partial w'}{\partial z}\right)\left\{\frac{\mathrm{d}}{\mathrm{d}z}\left(\frac{1}{|\mathrm{D}U|}\right)\right\}+\frac{\nabla^2 w'-\dfrac{\partial^2 w'}{\partial x^2}-\dfrac{\partial^2 u'}{\partial x\partial z}}{|\mathrm{D}U|}\right].\end{aligned} \tag{2.33}$$

The perturbation equations for the porous layer are expressed as

$$\frac{\partial u'_m}{\partial x_m}+\frac{\partial v'_m}{\partial y_m}+\frac{\partial w'_m}{\partial z_m}=0, \tag{2.34}$$

$$\frac{\partial u'_m}{\partial t_m} = -\left(\frac{\chi}{Re_m}\right)\left[\frac{\partial p'_m}{\partial x_m} + \frac{u'_m}{\delta^2 \eta_x}\right], \tag{2.35}$$

$$\frac{\partial v'_m}{\partial t_m} = -\left(\frac{\chi}{Re_m}\right)\left[\frac{\partial p'_m}{\partial y_m} + \frac{\xi_1 v'_m}{\delta^2 \eta_y}\right], \tag{2.36}$$

$$\frac{\partial w'_m}{\partial t_m} = -\left(\frac{\chi}{Re_m}\right)\left[\frac{\partial p'_m}{\partial z_m} + \frac{\xi_2 w'_m}{\delta^2 \eta_z}\right]. \tag{2.37}$$

It is known that Squire's transformation is not valid for Bingham fluids (Frigaard *et al.* 1994; Métivier & Nouar 2011). Thus, to perform stability analysis, we assume three-dimensional disturbances of the form

$$\left.\begin{gathered} u' = \hat{u}(z,t)\mathrm{e}^{\mathrm{i}(\alpha x+\beta y)}, \quad v' = \hat{v}(z,t)\mathrm{e}^{\mathrm{i}(\alpha x+\beta y)}, \quad w' = \hat{w}(z,t)\mathrm{e}^{\mathrm{i}(\alpha x+\beta y)}, \\ u'_m = \hat{u}_m(z_m,t_m)\mathrm{e}^{\mathrm{i}(\alpha_m x_m+\beta_m y_m)}, \quad v'_m = \hat{v}_m(z_m,t_m)\mathrm{e}^{\mathrm{i}(\alpha_m x_m+\beta_m y_m)}, \\ w'_m = \hat{w}_m(z_m,t_m)\mathrm{e}^{\mathrm{i}(\alpha_m x_m+\beta_m y_m)}, \\ p' = \hat{p}(z,t)\mathrm{e}^{\mathrm{i}(\alpha x+\beta y)}, \quad p'_m = \hat{p}_m(z_m,t_m)\mathrm{e}^{\mathrm{i}(\alpha x+\beta y)}, \quad h' = \hat{h}(t)\mathrm{e}^{\mathrm{i}(\alpha x+\beta y)}, \end{gathered}\right\} \tag{2.38}$$

where α and β are the real streamwise and spanwise wavenumbers, respectively. It is to be noted that yield stress fluids are unique in the sense that the yield surface also undergoes perturbation. Hence, perturbation in the yield surface is also being considered. Incorporation of the above disturbance expressions (2.38) in the governing perturbation equations (2.30)–(2.37) results in an initial value problem (the hats are dropped from u, v, etc., for convenience). Thus, in the following equations, u is essentially $\hat{u}$. Also, $\mathbb{Q} = \mathrm{D}^2 - (\alpha^2 + \beta^2)$. In addition, we write $\bar{u} = U$ for convenience in the following equations, wherever applicable.

For the fluid layer, the following set of equations is obtained:

$$0 = \mathrm{i}(\alpha u + \beta v) + \mathrm{D}w, \tag{2.39}$$

$$\frac{\partial u}{\partial t} = -\mathrm{i}\alpha U u - w\mathrm{D}U - \mathrm{i}\alpha p + \frac{1}{Re}\mathbb{Q}u + \frac{Bn}{Re}\left[\frac{-(\alpha^2+\beta^2)u - \mathrm{i}\alpha \mathrm{D}w}{|\mathrm{D}U|}\right], \tag{2.40}$$

$$\begin{aligned} \frac{\partial v}{\partial t} &= -\mathrm{i}\alpha U v - \mathrm{i}\beta p + \frac{1}{Re}\mathbb{Q}v \\ &\quad + \frac{Bn}{Re}\left[\frac{1}{|\mathrm{D}U|}\mathbb{Q}v + (\mathrm{D}v + \mathrm{i}\beta w)\left\{\mathrm{D}\left(\frac{1}{|\mathrm{D}U|}\right)\right\}\right], \end{aligned} \tag{2.41}$$

$$\begin{aligned} \frac{\partial w}{\partial t} &= -\mathrm{i}\alpha U w - \mathrm{D}p + \frac{1}{Re}\mathbb{Q}w \\ &\quad + \frac{Bn}{Re}\left[(2\mathrm{D}w)\left\{\mathrm{D}\left(\frac{1}{|\mathrm{D}U|}\right)\right\} + \frac{(\mathrm{D}^2-\beta^2)w - \mathrm{i}\alpha \mathrm{D}u}{|\mathrm{D}U|}\right]. \end{aligned} \tag{2.42}$$

For the porous layer, the following initial value problem is obtained:

$$\mathrm{i}(\alpha_m u_m + \beta_m v_m) + \mathrm{D}_p w_m = 0, \tag{2.43}$$

$$\frac{\partial u_m}{\partial t_m} = -\left(\frac{\chi}{Re_m}\right)\left[\frac{1}{\delta^2 \eta_x}u_m + \mathrm{i}\alpha_m p_m\right], \tag{2.44}$$

$$\frac{\partial v_m}{\partial t_m} = -\left(\frac{\chi}{Re_m}\right)\left[\frac{\xi_1}{\delta^2 \eta_y}v_m + \mathrm{i}\beta_m p_m\right], \tag{2.45}$$

$$\frac{\partial w_m}{\partial t_m} = -\left(\frac{\chi}{Re_m}\right)\left[\frac{\xi_2}{\delta^2\eta_z}w_m + \mathrm{D}_p p_m\right], \tag{2.46}$$

where $\xi_1 = K_x/K_y$ and $\xi_2 = K_x/K_z$ respectively denote the spanwise and normal anisotropy parameters. Also, $\mathrm{D}_p = \mathrm{d}/\mathrm{d}z_m$. The Reynolds numbers in the two layers are related as

$$Re = \hat{d}Re_m\left(\frac{l_2 + \dfrac{\bar{z}_{01}^2}{2}}{l_4\eta_x(0)}\right). \tag{2.47}$$

For modal analysis, the disturbance expressions in the governing perturbation equations (2.30)–(2.37) are replaced, using the following relations:

$$\left.\begin{gathered} u' = \hat{u}(z)\mathrm{e}^{\mathrm{i}(\alpha x+\beta y-ct)}, \quad v' = \hat{v}(z)\mathrm{e}^{\mathrm{i}(\alpha x+\beta y-ct)}, \quad w' = \hat{w}(z)\mathrm{e}^{\mathrm{i}(\alpha x+\beta y-ct)}, \\ u'_m = \hat{u}_m(z_m)\mathrm{e}^{\mathrm{i}(\alpha_m x_m+\beta_m y_m-c_m t_m)}, \quad v'_m = \hat{v}_m(z_m)\mathrm{e}^{\mathrm{i}(\alpha_m x_m+\beta_m y_m-c_m t_m)}, \\ w'_m = \hat{w}_m(z_m)\mathrm{e}^{\mathrm{i}(\alpha_m x_m+\beta_m y_m-c_m t_m)}, \\ p' = \hat{p}(z)\mathrm{e}^{\mathrm{i}(\alpha x+\beta y-ct)}, \quad z'_0 = \hat{z}_0(z)\mathrm{e}^{\mathrm{i}(\alpha x+\beta y-ct)}, \\ p'_m = \hat{p}_m(z_m)\mathrm{e}^{\mathrm{i}(\alpha_m x_m+\beta_m y_m-c_m t_m)}, \quad h' = \hat{h}(t)\mathrm{e}^{\mathrm{i}(\alpha x+\beta y)}. \end{gathered}\right\} \tag{2.48}$$

Thus, the following eigenvalue problem is obtained in the fluid and the porous layers:

$$0 = \mathrm{i}(\alpha u + \beta v) + \mathrm{D}w, \tag{2.49}$$

$$-\mathrm{i}cu = -\mathrm{i}\alpha Uu - w\mathrm{D}U - \mathrm{i}\alpha p + \frac{1}{Re}\mathbb{Q}u + \frac{Bn}{Re}\left[\frac{-(\alpha^2+\beta^2)u - \mathrm{i}\alpha\mathrm{D}w}{|\mathrm{D}U|}\right], \tag{2.50}$$

$$\begin{aligned} -\mathrm{i}cv \;=\; & -\mathrm{i}\alpha Uv - \mathrm{i}\beta p + \frac{1}{Re}\mathbb{Q}v \\ & + \frac{Bn}{Re}\left[\frac{1}{|\mathrm{D}U|}\mathbb{Q}v + (\mathrm{D}v + \mathrm{i}\beta w)\left\{\mathrm{D}\left(\frac{1}{|\mathrm{D}U|}\right)\right\}\right], \end{aligned} \tag{2.51}$$

$$\begin{aligned} -\mathrm{i}cw \;=\; & -\mathrm{i}\alpha Uw - \mathrm{D}p + \frac{1}{Re}\mathbb{Q}w \\ & + \frac{Bn}{Re}\left[(2\mathrm{D}w)\left\{\mathrm{D}\left(\frac{1}{|\mathrm{D}U|}\right)\right\} + \frac{(\mathrm{D}^2-\beta^2)w - \mathrm{i}\alpha\mathrm{D}u}{|\mathrm{D}U|}\right], \end{aligned} \tag{2.52}$$

$$\mathrm{i}(\alpha_m u_m + \beta_m v_m) + \mathrm{D}_p w_m = 0, \tag{2.53}$$

$$-\mathrm{i}c_m u_m = -\left(\frac{\chi}{Re_m}\right)\left[\frac{1}{\delta^2\eta_x}u_m + \mathrm{i}\alpha_m p_m\right], \tag{2.54}$$

$$-\mathrm{i}c_m v_m = -\left(\frac{\chi}{Re_m}\right)\left[\frac{\xi_1}{\delta^2\eta_y}v_m + \mathrm{i}\beta_m p_m\right], \tag{2.55}$$

$$-\mathrm{i}c_m w_m = -\left(\frac{\chi}{Re_m}\right)\left[\frac{\xi_2}{\delta^2\eta_z}w_m + \mathrm{D}_p p_m\right]. \tag{2.56}$$

At the yield surface (interface of yielded and unyielded zone), the following boundary conditions prevail:

$$\left.\begin{gathered} u(z_0) = 0, \quad v(z_0) = 0, \quad w(z_0) = 0, \\ \mathrm{D}u(z_0) = -h\mathrm{D}^2U(z_0), \quad \mathrm{D}v(z_0) = 0, \quad \mathrm{D}w(z_0) = 0. \end{gathered}\right\} \tag{2.57}$$

Other boundary conditions are obtained from the Beavers–Joseph condition at the fluid–porous interface, along with the continuity of normal and spanwise velocity, and pressure.

Thus, at the fluid–porous interface ($\bar{z} = \bar{z}_m = 0$), we have

$$\left.\begin{aligned} \mathrm{D}u(0) &= \frac{\alpha_{BJ}\hat{d}}{\delta\sqrt{\eta_x(0)}}\left[u(0) - \frac{\hat{d}Re_m}{Re}u_m(0)\right], \\ Re\, v(0) &= \hat{d}Re_m v_m(0), \\ Re\, w(0) &= \hat{d}Re_m w_m(0), \\ p(0) &= \frac{\hat{d}^2}{Re}Re_m p_m(0). \end{aligned}\right\} \tag{2.58}$$

At the bottom surface of the porous layer ($z = -d_m$, or $\bar{z}_m = -1$), we have

$$v_m(-1) = 0, \quad w_m(-1) = 0. \tag{2.59a,b}$$

The following relation exists among the wavenumbers ($\alpha, \alpha_m, \beta, \beta_m$) in the fluid and porous layers:

$$\alpha = \hat{d}\alpha_m, \quad \beta = \hat{d}\beta_m. \tag{2.60a,b}$$

Equations (2.49)–(2.56) are second order in u, v, w, and first order in w_m, p, p_m. For solving the same, we are seemingly using 12 boundary conditions (2.57)–(2.59). In other words, the system is apparently over-specified. However, a careful observation will reveal the reality that is typical of yield stress fluids. In (2.57), the relation for Du essentially specifies the condition for the amplitude of the perturbation of the yield surface. Thus, the relation basically defines h, and not u. The relations for Dv and Dw are also required, as they take care of the singularity of $|\mathrm{D}U|^{-1}$ as the yield surface is approached. The same has been elucidated by other researchers as well (Frigaard & Nouar 2003; Nouar *et al.* 2007).

It may be highlighted here that the disturbance waves arising in the fluid and porous layers are the same, i.e. they have the same wavelength. As a result, the dimensional wavenumbers, being the reciprocal of wavelength, are also the same in the two layers. However, in our analysis, we are considering non-dimensional wavenumbers, namely α in the fluid layer and α_m in the porous layer: α is non-dimensionalized with respect to d (thickness of the fluid layer), while α_m is made non-dimensional with respect to d_m (thickness of the porous layer). Thus, $\alpha \neq \alpha_m$ (in fact, $\alpha = \hat{d}\alpha_m$, as already stated; in fact, $\beta = \hat{d}\beta_m$ as well). In a similar way, the non-dimensional distances in the two layers are related as $\hat{d}x = x_m$ and $\hat{d}y = y_m$. Thus, the Fourier expressions are identical in the two layers, i.e. $\mathrm{e}^{\mathrm{i}(\alpha x+\beta y-ct)} = \mathrm{e}^{\mathrm{i}(\alpha_m x_m+\beta_m y_m-c_m t_m)}$. The modal expressions u and u' differ in the z direction, which is logical, as the base profiles are also different in the two layers. These assumptions are in conformity with earlier studies (Chang *et al.* 2006; Hill & Straughan 2008; Deepu *et al.* 2015; Chang *et al.* 2017).

2.6. *Numerical solution*

We have assumed porosity $\chi = 0.1$ throughout. Unless otherwise explicitly specified, the parameters assume the following values: $Bn = 0.2$, $\beta_0 = 0.016$, $\hat{d} = 0.3$, $\alpha_{BJ} = 0.2$, $\delta = 0.001$, $\xi_1 = 2$, $\xi_2 = 2$ and $A_{inh} = 2$. For modal analysis, the resultant generalized

eigenvalue problem of the form $\boldsymbol{AX} = c\boldsymbol{BX}$ is solved via the Chebyshev spectral collocation method using QZ decomposition. Here, $\boldsymbol{X} = (u, v, w, p)$, and $\boldsymbol{A}$ and $\boldsymbol{B}$ are the matrices comprising Chebyshev derivatives. The discretization of the equations is carried out on the Gauss–Lobatto grid, consisting of $(N + 1)$ collocation points. The details of the spectral collocation method using Chebyshev polynomials have been discussed by Schmid & Henningson (2001). MATLAB 2014b software was used for the computation. The calculations were checked with increasing number of Chebyshev polynomials ($N = 32$, 64, 96, 128, 192, 256, 384, 512). It was observed that for $N = 192$, the first 50 eigenvalues (sorted in terms of increasing imaginary part) gave accuracy up to five digits. In other words, the first five digits remained invariant with further increase in N. Hence, all the computations reported in this paper were carried out with $N = 192$.

2.7. *Non-modal analysis and energy growth*

For non-modal analysis, the following linear initial value problem needs to be solved:

$$\frac{\partial}{\partial t}\boldsymbol{q} = -\mathrm{i}\boldsymbol{L}\boldsymbol{q}, \tag{2.61}$$

where $\boldsymbol{q}$ is expressed as $\boldsymbol{q} = (\hat{u}, \hat{v}, \hat{w}, \hat{p})^{\mathrm{T}}$, and $\boldsymbol{L}$ is defined as $\boldsymbol{L} = -\mathrm{i}\boldsymbol{B}^{-1}\boldsymbol{A}$. The solution is expressed as $\boldsymbol{q}(t) = \boldsymbol{q}(0)\exp(-\mathrm{i}\boldsymbol{L}t)$, where $\boldsymbol{q}(0)$ is the initial value of the perturbation variables.

2.7.1. *Response to initial conditions: growth function*

In the above context, the growth function defines the maximum possible amplification of the initial condition, and is mathematically expressed as

$$G(t) = \max_{q(0)\neq 0} \frac{\|\boldsymbol{q}(t)\|^2}{\|\boldsymbol{q}(0)\|^2} = \|\exp(-\mathrm{i}\boldsymbol{L}t)\|^2, \tag{2.62}$$

where $\|\cdot\|$ is the norm.

In general, for a flow stability problem, if the Reynolds number Re is less than the critical energy Reynolds number Re_1, then the growth function $G(t)$ is never greater than unity, i.e. $G_{max} = 1$. In such a case, optimal time t_{opt} is zero. On the other hand, if the Reynolds number is greater than the critical Reynolds number Re_2, then one of the eigenvalues of the linear Orr–Sommerfeld operator has a positive imaginary part, and the flow becomes unstable. Mathematically, the growth function becomes unbounded at infinite time. In the case of $Re_1 < Re < Re_2$, modal analysis yields no unstable eigenvalue and thus the flow is linearly stable. However, a transient growth is observed which decays with time. For the current work, stability analysis is performed for a vast range of Reynolds numbers, but no unstable eigenvalues are obtained. Thus, for analysing non-modal behaviour, a Reynolds number higher than the critical energy Reynolds number Re_1 is taken into consideration.

2.7.2. *Response to external excitations: resolvent*

Let us assume that a flow configuration is subjected to an input signal V, represented as

$$V(x, y, z, t) = \exp(-\mathrm{i}\omega t)v(x, y, z), \tag{2.63}$$

where ω is the frequency of V, and ω is assumed to be complex. Then, the relationship among the input signal V and the response U is given by the following differential equation:

$$\frac{\mathrm{d}U}{\mathrm{d}t} = -\mathrm{i}\boldsymbol{L}U + \exp(-\mathrm{i}\omega t)v. \tag{2.64}$$

Solution of the above equation leads to the following expression for U:

$$U(x, y, z, t) = \mathrm{i}\exp(-\mathrm{i}\omega t)u = \mathrm{i}\exp(-\mathrm{i}\omega t)(\omega \boldsymbol{I} - \boldsymbol{L})^{-1}v. \tag{2.65}$$

In the above relation, $\boldsymbol{I}$ is the identity matrix, and $(\omega \boldsymbol{I} - \boldsymbol{L})^{-1}$ is referred to as the resolvent; $\boldsymbol{L}$ has already been defined earlier. For an input signal of frequency ω, the maximum amplification of the external excitation, $R(\alpha, \beta, \omega)$, is given by the norm of the resolvent operator. Thus,

$$R(\alpha, \beta, \omega) = \max_{v \neq 0} \frac{\|u\|}{\|v\|} = \|(\omega \boldsymbol{I} - \boldsymbol{L})^{-1}\|, \tag{2.66}$$

where $\boldsymbol{I}$ is the identity matrix, and ω is the eigenvalue of $\boldsymbol{L}$, such that $\|(\omega \boldsymbol{I} - \boldsymbol{L})^{-1}\| \rightarrow \infty$. In mathematical terms, the resolvent norm is equivalent to amplification of the response under external forcing. In this context, it is essential to discuss the definition of the 'ε-pseudospectrum'. A basic understanding of the pseudospectrum is critical to non-modal stability analysis. For any $\varepsilon \geqslant 0$, the pseudospectrum of $\boldsymbol{L}$ is defined as (Trefethen & Embree 2005)

$$\Lambda_\varepsilon(\boldsymbol{L}) = \{\omega \in \mathbb{C} : \|(\omega \boldsymbol{I} - \boldsymbol{L})^{-1}\| \geqslant \varepsilon^{-1}\}. \tag{2.67}$$

With a variation in ε, contours of pseudospectra are obtained. When $\varepsilon = 0$, the pseudospectrum reduces to the spectrum, i.e. the set of eigenvalues obtained from normal mode analysis. Thus, with increasing ε, there is deviation from the traditional eigenvalue analysis. In a non-modal stability analysis problem, there are two major components that need to be explored. One is the response of the system to external excitations, the other being the transient growth of the initial conditions. The resolvent norm describes the maximum possible amplification in response to external excitations. On the other hand, transient growth of the initial conditions is expressed by the growth function $G(t)$. In the current study, we have considered only the response to initial conditions, i.e. $G(t)$. The pseudospectrum has been studied only in the limiting case of Newtonian fluids, in order to validate our simulation methodology with that of the existing literature.

2.8. *Energy stability*

For carrying out energy stability analysis, the perturbation kinetic energy is quantified as

$$\begin{aligned} E = {} & \frac{\alpha\beta}{8\pi^2}\left[\frac{1}{z_0}\int_0^{z_0}\int_0^{2\pi/\alpha}\int_0^{2\pi/\beta}(u_r'^2 + v_r'^2 + w_r'^2)\,\mathrm{d}y\,\mathrm{d}x\,\mathrm{d}z\right] \\ & + \frac{\alpha_m\beta_m}{8\pi^2}\left[\int_{-1}^{0}\int_0^{2\pi/\alpha_m}\int_0^{2\pi/\beta_m}(u_{mr}'^2 + v_{mr}'^2 + w_{mr}'^2)\,\mathrm{d}y_m\,\mathrm{d}x_m\,\mathrm{d}z_m\right], \end{aligned} \tag{2.68}$$

where $u_r' = \mathrm{Real}(\hat{u}(z,\, t)\mathrm{e}^{\mathrm{i}(\alpha x+\beta y)})$, $u_{mr}' = \mathrm{Real}(\hat{u}_m(z_m,\, t_m)\mathrm{e}^{\mathrm{i}(\alpha_m x_m+\beta_m y_m)})$, and so on. No energy growth is possible if $\mathrm{d}E/\mathrm{d}t < 0$ as $t \to \infty$ (Butler & Farrell 1992). Thus, the condition for no energy growth may be expressed as

$$\frac{1}{Re_1} = \sup_{\boldsymbol{u}} \frac{\boldsymbol{I}_1(\boldsymbol{u})}{\boldsymbol{I}_2(\boldsymbol{u}) + \boldsymbol{I}_3(\boldsymbol{u})}, \tag{2.69}$$

with

$$\boldsymbol{I}_1(\boldsymbol{u}) = -(\langle (u_r w_r + u_i w_i)\mathrm{D}U\rangle + [\![(u_{mr} w_{mr} + u_{mi} w_{mi})\mathrm{D}U]\!]), \tag{2.70}$$

$$\boldsymbol{I}_2(\boldsymbol{u}) = \langle |\mathrm{D}\boldsymbol{u}|^2 + (\alpha^2+\beta^2)|\boldsymbol{u}|^2\rangle + [\![|\mathrm{D}\boldsymbol{u}_m|^2 + (\alpha_m^2+\beta_m^2)|\boldsymbol{u}_m|^2]\!], \tag{2.71}$$

$$\begin{aligned}\boldsymbol{I}_3(\boldsymbol{u}) \;=\; Bn \Bigg[&\left\langle \frac{3|\mathrm{D}w|^2 + (\alpha^2+\beta^2)|u|^2}{|\mathrm{D}U|} \right\rangle \\ &+ \left\langle \frac{(\alpha^2+\beta^2)|\alpha u - \mathrm{i}\mathrm{D}w|^2 + |\alpha \mathrm{D}u - \mathrm{i}(\mathrm{D}^2 w + \beta w)|^2}{\beta^2 |\mathrm{D}U|} \right\rangle \Bigg].\end{aligned} \tag{2.72}$$

In the above expressions, the following terminology is applicable:

$$\left.\begin{aligned} |u|^2 = u_r^2 + u_i^2, \quad |\boldsymbol{u}|^2 = |u|^2 + \left|\frac{-\alpha u + \mathrm{i}\mathrm{D}w}{\beta}\right|^2 + |w|^2, \\ \langle\cdot\rangle = \int_0^{z_0} (\cdot)\,\mathrm{d}z, \quad [\![\cdot]\!] = \int_{-1}^{0} (\cdot)\,\mathrm{d}z_m, \end{aligned}\right\} \tag{2.73}$$

and u_r and u_i are the real and imaginary components of the perturbation. The corresponding variational problem needs to be solved. The Euler equations for the same may be given as

$$\begin{aligned}&(\mathrm{D}^2 - \alpha^2 - \beta^2)^2 w \\ &\quad + Bn \left[-4(\alpha^2+\beta^2)\mathrm{D}\left(\frac{\mathrm{D}w}{|\mathrm{D}U|}\right) - \mathrm{i}(\mathrm{D}^2 + \alpha^2 + \beta^2)\left\{\frac{\mathrm{D}(-\alpha u + \mathrm{i}\mathrm{D}w) + \mathrm{i}\beta^2 w}{|\mathrm{D}U|}\right\}\right] \\ &= -\frac{\lambda}{2}[(\alpha^2+\beta^2)u\mathrm{D}U + \mathrm{i}\alpha\mathrm{D}(w\mathrm{D}U)],\end{aligned} \tag{2.74}$$

$$\begin{aligned}&(\alpha^2+\beta^2)(\mathrm{D}^2 - \alpha^2 - \beta^2)u - \mathrm{i}\alpha\mathrm{D}(\mathrm{D}^2 - \alpha^2 - \beta^2)w - Bn \\ &\qquad \times \left[\frac{(\alpha^2+\beta^2)^2 u - \mathrm{i}\alpha^3 \mathrm{D}w}{|\mathrm{D}U|} + \alpha\mathrm{D}\left(\frac{\mathrm{D}(\mathrm{i}\mathrm{D}w - \alpha u)}{|\mathrm{D}U|}\right)\right] \\ &\qquad = \frac{\lambda\beta^2}{2} w\mathrm{D}U,\end{aligned} \tag{2.75}$$

$$\begin{aligned}&\frac{1}{\delta^2}\left[\frac{\mathrm{D}_p^2 u_m}{\eta_x} - \left(\frac{\xi_1\alpha_m^2}{\eta_y} + \frac{\xi_2\beta_m^2}{\eta_z}\right)(u_m + \mathrm{i}\mathrm{D}_p w_m) - \frac{\mathrm{D}_p\eta_x\mathrm{D}_p(u_m + \mathrm{i}\mathrm{D}_p w_m)}{\eta_x^2}\right] \\ &\quad = \frac{\mathrm{i}\lambda}{\hat{d}\chi}\left(\frac{l_4\eta_x(0)}{l_2 + \dfrac{\bar{z}_{01}^2}{2}}\right)(\mathrm{D}_p^2 - \alpha_m^2 - \beta_m^2)(u_m + \mathrm{i}\mathrm{D}_p w_m).\end{aligned} \tag{2.76}$$

The above eigenvalue problem in λ is solved subject to the following boundary conditions:

$$\left.\begin{gathered} u(z_0)=0, \quad w(z_0)=0, \quad \mathrm{D}w(z_0)=0, \\ \mathrm{D}u(0)=\frac{\alpha_{BJ}\hat{d}}{\delta\sqrt{\eta_x(0)}}\left[u(0)-\frac{\hat{d}Re_m}{Re}u_m(0)\right], \quad Re\,w(0)=\hat{d}Re_m w_m(0), \quad \mathrm{D}w_m(0)=0, \\ u_m(-1)=0, \quad w_m(-1)=0, \quad \mathrm{D}w_m(-1)=0. \end{gathered}\right\} \tag{2.77}$$

As already emphasized earlier, the solution gives the conditions for no energy growth. The solution methodology for this eigenvalue problem set is also Chebyshev spectral collocation (presented in § 2.6). The results are discussed subsequently in § 3.4.

3. Results and discussion

3.1. *Validation*

For the purpose of validation, we compare our findings with two different studies (both modal and non-modal) reported in the literature, in the limiting cases. First, we compare our non-modal results with that obtained for Poiseuille flow of a Newtonian fluid. As discussed in the preceding section, the pseudospectrum for Poiseuille flow of a Newtonian fluid ($Bn = 0$) is constructed in order to validate our findings with the literature. The same is depicted in figure 2(*a*,*b*). Both streamwise ($\alpha \neq 0, \ \beta = 0$) as well as spanwise ($\alpha = 0, \ \beta \neq 0$) perturbations are considered at $Re = 3000$. It is found that the response to streamwise perturbation is a spectrum consisting of the A, P and S branches. On the other hand, the spectrum for the spanwise perturbation is a single vertical branch. Our results coincide with those of Reddy & Henningson (1993), thereby validating the current numerical approach. In addition, we have also validated our modal stability results with Poiseuille flow of a Newtonian fluid overlying a porous layer, as reported by Chang *et al.* (2006). Figure 2(*c*) shows the neutral stability curve in the case of streamwise perturbation for the set ($Bn = 0$, $A_{inh} = 0$, $K_y = 1$, $K_z = 1$). The neutral stability results reported in the literature by Chang *et al.* (2006) are also displayed on the same plot (figure 2*a* in Chang *et al.* 2006). As evident from the figure, they show a satisfactory match.

3.2. *Variation of* $\bar{z}_{01}$ *and* $\bar{z}_{02}$

As already discussed in the beginning, the existence of a plug zone is a characteristic feature of yield stress fluids. The thickness of the plug zone can be determined from the location of yield surfaces, $\bar{z}_{01}$ and $\bar{z}_{02}$. Thus, studying the variations of $\bar{z}_{01}$ and $\bar{z}_{02}$ with various parameters can provide useful insight into flow characteristics. Figure 3 demonstrates the effect of Bingham number, as well as various porous layer parameters, on $\bar{z}_{01}$ and $\bar{z}_{02}$. Figure 3(*a*) shows that, although the variations of both $\bar{z}_{01}$ and $\bar{z}_{02}$ are monotonic with Bn, the trends are opposite to each other. The lower yield surface $\bar{z}_{01}$ reduces with Bn, unlike $\bar{z}_{02}$, which increases monotonically. Physically, this represents widening of the plug zone with Bn. The values of $\bar{z}_{01}$ and $\bar{z}_{02}$ coincide at $Bn = 0$, indicating no plug zone (Newtonian fluid). Essentially, as yield stress increases, there is a gradual transition from single shear (Newtonian) to double shear flow with a plug zone in the middle. Figure 3(*b*,*c*) reveals that both $\bar{z}_{01}$ and $\bar{z}_{02}$ increase with depth ratio $\hat{d}$ and slip parameter α_{BJ}. However, there is saturation at higher values of $\hat{d}$ and α_{BJ}. Increase in α_{BJ} translates to rise in velocity

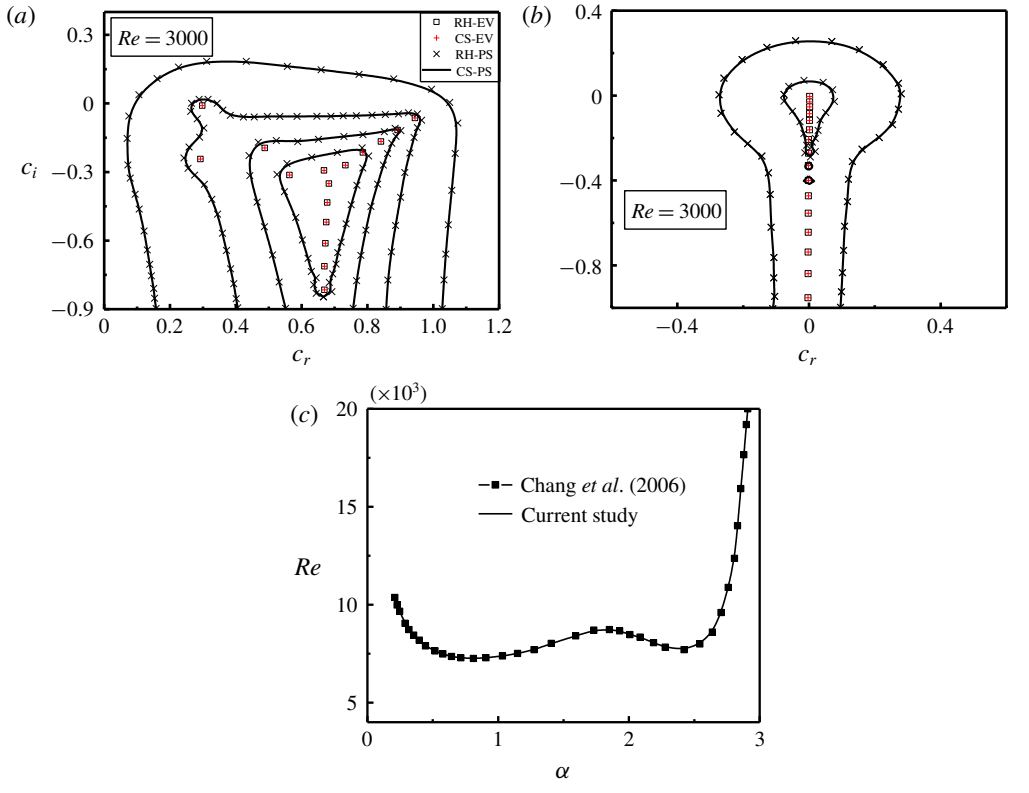

FIGURE 2. (Colour online) Validation with literature. (*a*,*b*) Comparison with Reddy & Henningson (1993) for (*a*) streamwise ($\alpha = 1,\ \beta = 0$) and (*b*) spanwise ($\alpha = 0,\ \beta = 2$) perturbations. (*c*) Comparison with Chang *et al.* (2006) for $Bn = 0$. For (*a*), the boundaries of the ε-pseudospectra from outer to inner are $\varepsilon = 10^{-1},\ 10^{-2},\ 10^{-3},\ 10^{-4}$. For (*b*), they are $\varepsilon = 10^{-1},\ 10^{-2}$. In (*a*,*b*), the legend denotes the following: RH-EV, eigenvalues reported by Reddy & Henningson (1993); CS-EV, eigenvalues obtained in the current study; RH-PS, pseudospectra reported by Reddy & Henningson (1993); CS-PS, pseudospectra obtained in the current study.

gradient at the fluid–porous interface. This results in higher momentum transfer in the transverse direction, leading to plug behaviour in the upper shear zone and a more pronounced lower shear zone, represented by an upward shift of both the yield surfaces (Sengupta & De 2019). Of course, there cannot be prolonged monotonic rise of the interface velocity gradient, leading to saturation at higher values of α_{BJ}. As per the Beavers–Joseph condition, depth ratio is also proportional to the interface velocity gradient, thereby exhibiting similar trend as that of α_{BJ}. As shown in figure 3(*d*), the trend is reverse for δ. Darcy number represents the permeability of the porous layer. As the porous layer becomes more permeable, the porous layer velocity increases. Thus, there is a reduction in the velocity gradient at the fluid–porous interface, resulting in a downward shift of the yield surfaces with δ. In figure 3(*e*), the yield surfaces exhibit an asymmetric variation with inhomogeneity factor A_{inh} with respect to $A_{inh} = 0$, in addition to being non-monotonic. For $A_{inh} > 0$, there is a reduction in the values of $\bar{z}_{01}$ and $\bar{z}_{02}$. Increase in inhomogeneity amounts to increase in overall

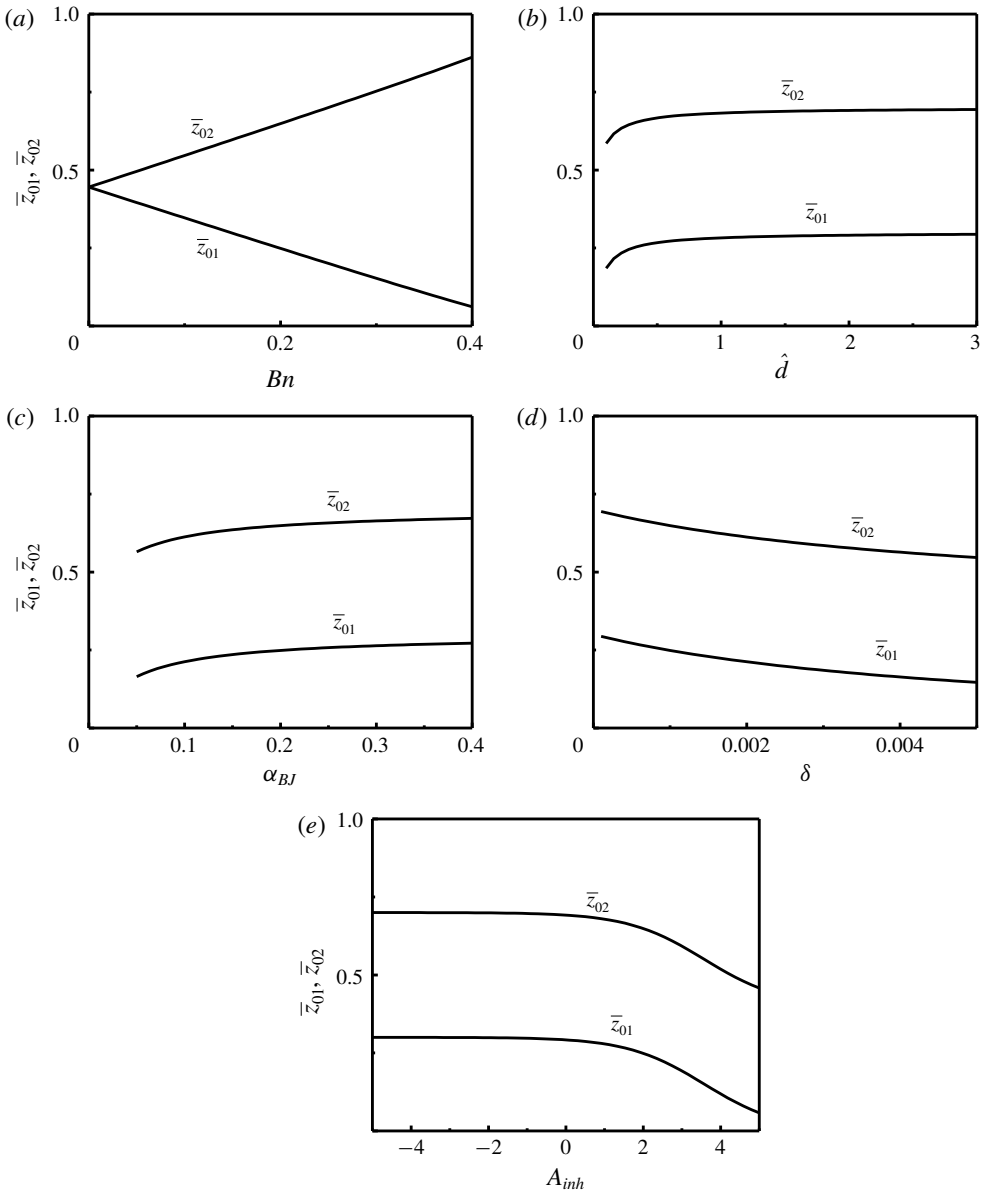

FIGURE 3. Variation of $\bar{z}_{01}$ and $\bar{z}_{02}$ with various parameters: (*a*) Bingham number; (*b*) depth ratio; (*c*) slip coefficient; (*d*) Darcy number; and (*e*) inhomogeneity factor.

permeability of the porous medium. Owing to this, the trend of a downward shift in the yield surfaces with A_{inh} somewhat resembles the behaviour of δ. High negative values of A_{inh} indicate drastic (exponential) reduction in the permeability, due to which the fluid–porous interface almost behaves as an impermeable wall. Thus, the porous layer no longer affects the location of the yield surfaces, due to which both $\bar{z}_{01}$ and $\bar{z}_{02}$ become almost invariant at large negative A_{inh}.

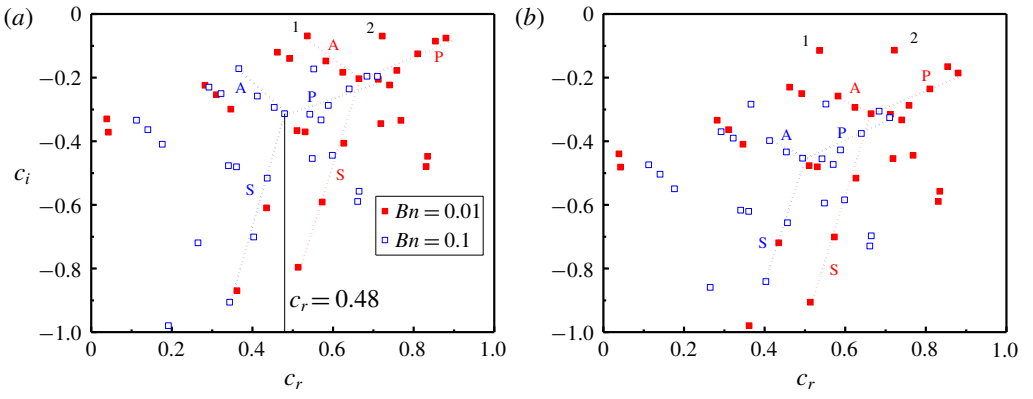

FIGURE 4. (Colour online) Eigenvalue spectra studying the effect of depth ratio $\hat{d}$: (*a*) $\hat{d} = 0.1$ and (*b*) $\hat{d} = 1$. Dotted lines represent the oblique branches.

3.3. *Eigenvalue spectra*

The dependence of the normal modes on *Bn* is shown in figures 4–6, in addition to the effect of the various parameters of the porous layer. It is observed that increase in *Bn* from 0.01 to 0.1 leads to reduction in c_i. However, there is no value of $c_i > 0$ in each of the cases. Unlike non-porous channel shear flow, there is no vertical S branch here. Instead, there is an oblique branch at approximately $c_r = 0.48$ (the oblique line is represented by dotted line in figure 4*a*). The complex interplay of the fluid and porous modes makes the branches oblique. Also, two distinct branches can be located on either side of this oblique line, similar to A and P branches of non-porous Newtonian flow. Reduction in the value of c_i is due to the increase in the viscoplasticity of the fluid with *Bn*. Thus, the flow becomes increasingly stable with increased *Bn* (even though it is never linearly unstable).

Figures 4–6 explore the effects of the porous layer parameters on the spectra. The P and S branches are not very sharp, unlike the case of non-porous flow configuration. Although these A and P branches are diffused, there is an interesting observation regarding the imaginary part of the eigenvalues. To explain the same, let us observe the two modes marked 1 and 2 in figure 4(*a*). Their coordinates in figure 4(*a*) are as follows: mode 1 (0.53624, −0.06912) and mode 2 (0.72222, −0.06976). Thus, for $\hat{d} = 0.1$, mode 1 would dominate the transition behaviour. But as $\hat{d}$ is increased to 1 in figure 4(*b*), the coordinates for the two modes are: mode 1 (0.53624, −0.11480) and mode 2 (0.72222, −0.11411). So, mode 2 becomes dominant in this case. Thus, with increase in depth ratio from 0.1 to 1, there is a 'switching' of the modes carrying the maximum value of c_i, from mode 1 to mode 2. Similar behaviour of mode switching is also observed in the case of slip parameter and permeability, depicted in figures 5 and 6. Thus, slip parameter and permeability also induce mode switching in the eigenvalue spectra. However, the mode switching is not explicitly demonstrated in figures 5 and 6, to avoid repetition. The mode switching phenomenon leads to the development of unique behaviour in the neutral curves, as discussed later in § 3.4.

3.3.1. *Effect of the porous modes*

In order to have a better understanding of the effect of viscoplasticity on porous modes, the effect of *Bn* on the eigenfunction is studied. As demonstrated in figure 7,

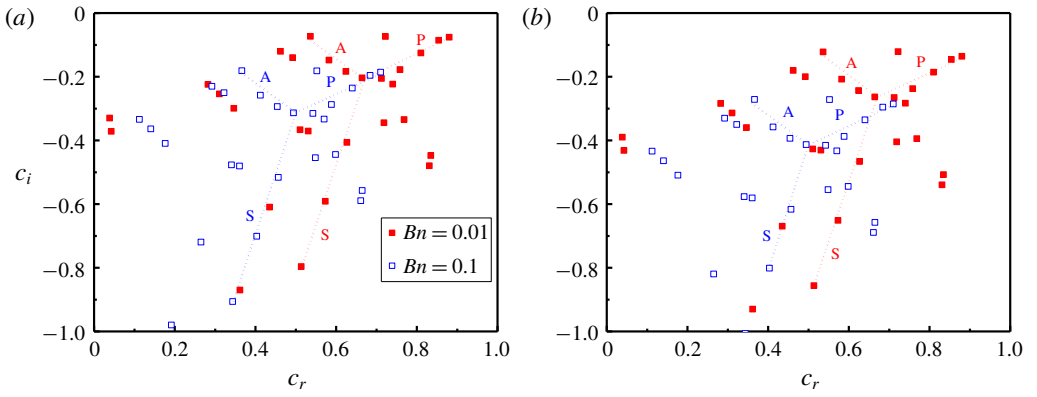

FIGURE 5. (Colour online) Eigenvalue spectra studying the effect of slip parameter α_{BJ}: (*a*) $\alpha_{BJ} = 0.1$ and (*b*) $\alpha_{BJ} = 0.4$. Dotted lines represent the oblique branches.

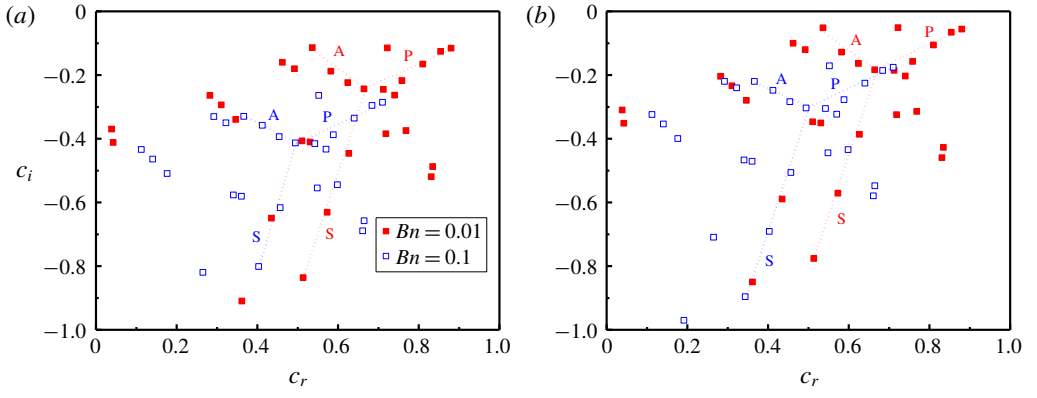

FIGURE 6. (Colour online) Eigenvalue spectra studying the effect of Darcy number δ: (*a*) $\delta = 0.0001$ and (*b*) $\delta = 0.001$. Dotted lines represent the oblique branches.

for low Bn ($Bn = 0.01$), there is a flow reversal near the interface. Also, there is significant protrusion of the momentum into the porous layer. With gradual increase in Bn to $Bn = 0.05$, the degree of protrusion reduces. The extent of flow reversal is also less. But both these effects of flow reversal and protrusion are exhibited at this stage. However, with further increase in Bn to 0.1, there is no more protrusion. Only flow reversal near the interface is observed. For higher Bn ($Bn = 0.2$), even the flow reversal ceases to exist. All these effects reveal the effect of the porous layer in deciding the mode of stability. At lower Bn, Newtonian flow characteristics are more dominant. Thus, there is significant perturbation in the porous layer as well, in addition to the fluid layer. This is the cause of the flow reversal and protrusion in figure 7(*a*,*b*). At this stage, the effects of the fluid layer and the porous layer on flow transition are comparable. As Bn further increases to 0.1, the protrusion of the perturbation becomes negligible, owing to the onset of yield stress effects. At even higher Bn, the viscoplastic effects dominate the porous layer completely. As a result, the porous layer is unable to influence the transition behaviour. The dominant role is now played by the fluid layer alone.

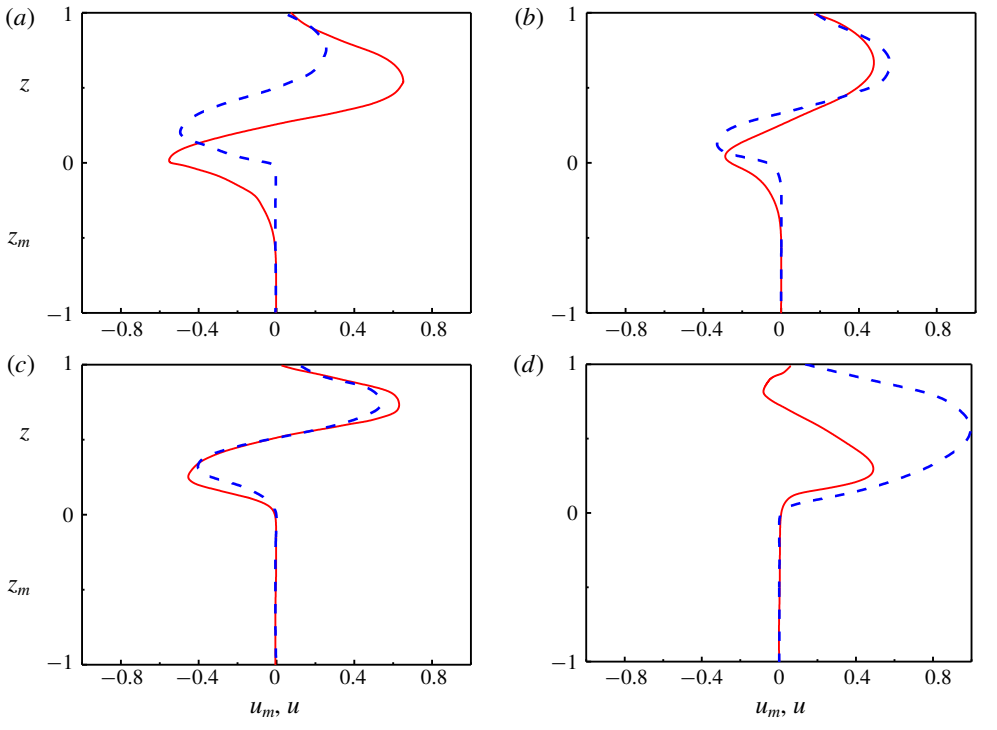

FIGURE 7. (Colour online) Variation of the eigenfunctions with Bn: (*a*) $Bn = 0.01$; (*b*) $Bn = 0.05$; (*c*) $Bn = 0.1$; and (*d*) $Bn = 0.2$. Here u_m is the eigenfunction corresponding to the domain $-1 \leqslant z_m \leqslant 0$, whereas u is the eigenfunction corresponding to the domain $0 \leqslant z \leqslant 1$. Solid lines refer to the real components, while the dashed lines refer to the imaginary components.

3.4. *Non-modal analysis*

3.4.1. *Neutral stability*

As already discussed, in the current study, modal analysis did not yield any unstable eigenvalue for $Bn > 0$. Thus, non-modal study is attempted in order to investigate the possible sources of perturbation amplifications. First, the conditions for no energy growth are explored, i.e. when $G(t)$ is never greater than unity. Therefore, in figure 8(*a–f*), the neutral stability curves are constructed for critical energy Reynolds number Re_1 versus the spanwise disturbances β. Spanwise disturbances are selected, as they have been found to be the source of greater amplification of perturbations (Reddy & Henningson 1993; Liu & Liu 2014; Liu *et al.* 2018). It is observed that the curves are multimodal, as opposed to the unimodal curves obtained for flow of viscoplastic fluids in a non-porous environment (Liu *et al.* 2018). The additional modes are imparted by the existence of the porous layer. Figure 8(*a*) delineates the effect of depth ratio $\hat{d}$ on critical energy Reynolds number. It is found that, with increase in the depth ratio from 0.1 to 3, there is a shift in the dominant mode of critical Re_1 towards long-wave (i.e. small-β) perturbations. This exhibition of multimodal behaviour can be traced back to the phenomenon of mode switching, as discussed in § 3.3. Mode switching leads to multiple critical points in the neutral curve, dictated by the relative influence of the fluid layer and porous layer modes. The

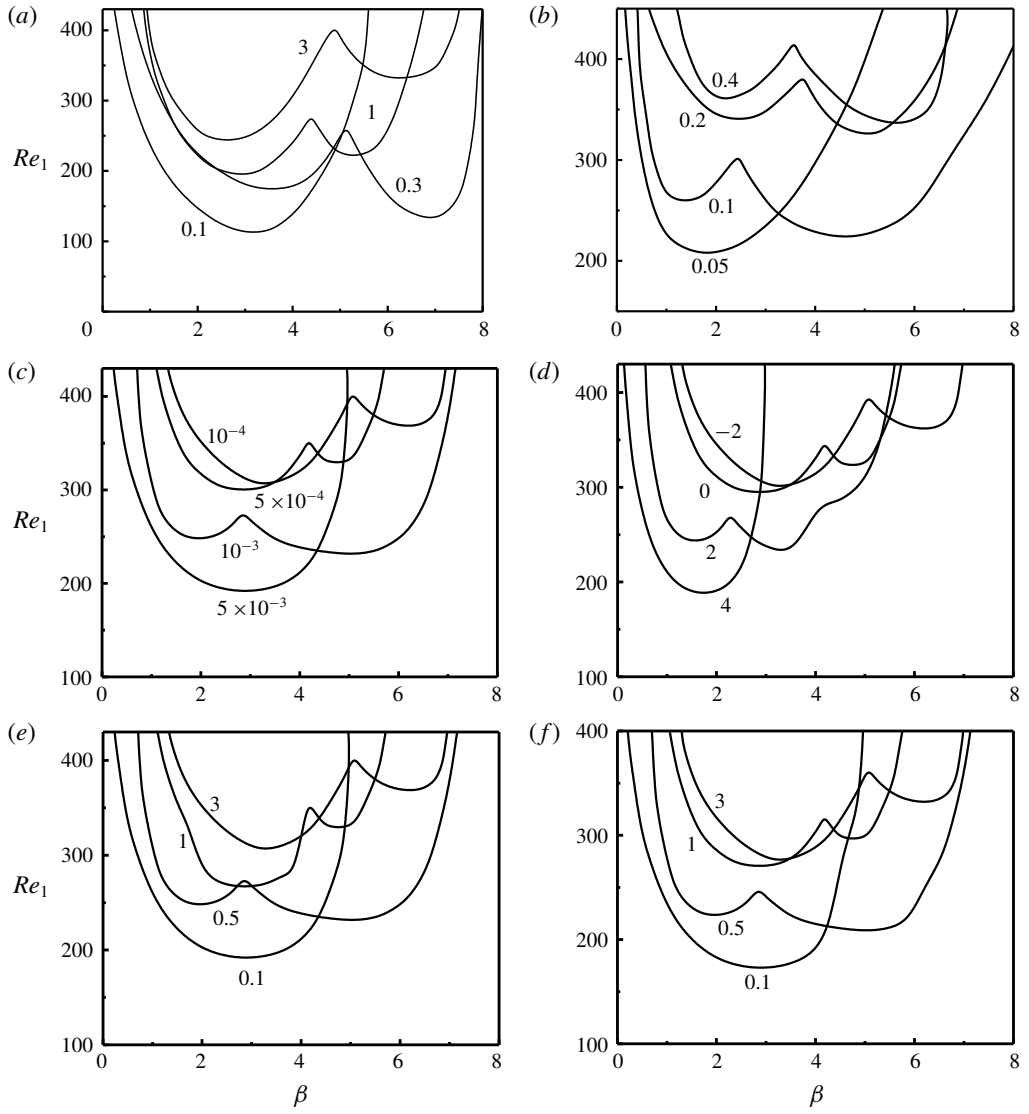

FIGURE 8. Plots of energy Reynolds number versus spanwise wavenumber ($\alpha = 0$) to depict the effects of: (*a*) depth ratio $\hat{d}$; (*b*) slip parameter α_{BJ}; (*c*) Darcy number δ; (*d*) inhomogeneity factor A_{inh}; (*e*) spanwise anisotropy parameter ξ_1; and (*f*) normal anisotropy parameter ξ_2. The numbers in the panels denote the respective values of the parameters. Here $Bn = 0.2$ in all cases.

complex interaction between the porous and fluid modes decides the dominant mode of instability, depending on the value of the porous layer parameters. Figure 8(*b*) demonstrates the effect of the Beavers–Joseph coefficient α_{BJ}, which is essentially a slip parameter. As slip parameter increases from 0.2 to 0.4, the fluid layer mode dominates the criticality. The only difference is that, at higher values of slip parameter ($\alpha_{BJ} > 0.2$), the shifting of dominant modes is less significant. As far as the effect of the permeability (in terms of Darcy number) is concerned, it depicts an opposite

trend. Thus, the long-wave perturbation is dominant with increasing permeability. With higher Darcy number, the critical energy Reynolds number is lowered. This is because with lower permeability there is a greater flow resistance in the porous layer. As a result, more fluid is pushed into the fluid layer, establishing the dominance of the fluid layer mode in deciding the stability of the system. The effect of the inhomogeneity factor A_{inh} is depicted in figure 8(*d*). Porous layer modes are found to be dominant with A_{inh}. This is possibly because an increase in A_{inh} is found to lower the value of $\bar{z}_{01}$ significantly for $A_{inh} > 0$ (figure 3), leading to the porous modes becoming more prominent. Also, there is a monotonic lowering of criticality with A_{inh} due to the prominence of porous modes. Thus, inhomogeneity acts as a destabilizing agent. The effects of anisotropy factors ξ_1 and ξ_2 on the transition behaviour are depicted in figure 8(*e*,*f*). The criticality is found to lower with decrease in the anisotropic parameters. Decrease in anisotropic parameters implies relative increase in the values of K_y and K_z. Thus, the permeabilities enhance in the spanwise and normal directions. This increases the total volume of fluid flowing through the porous layer, for a fixed K_x. This increased volume of fluid contributes to the momentum enhancement in the porous layer, and thus, is responsible for the lowering of criticality. Thus, the anisotropy parameters generally aid stabilization of flow.

3.4.2. *Growth rate*

Figure 9 shows the effects of the porous layer parameters on the growth rate curves for a spanwise perturbation. It is observed that, with increase in depth ratio in figure 9(*a*), the maximum possible growth as well as the time corresponding to maximum growth is reduced. However, beyond $\hat{d} = 1$, the reduction is not substantial. The slip parameter also depicts a similar tendency in figure 9(*b*), but the reduction in $G(t)$ is significant even at high slip coefficient, i.e. at high velocity gradient at the fluid–porous interface. As far as permeability is concerned in figure 9(*c*), increase in Darcy number leads to monotonic increase in the maximum growth, as well as the time of maximum growth. These effects illustrate the relative roles played by each of the porous layer parameters in deciding the non-modal growth. With increase in depth ratio, the fluid layer gradually grows in thickness. Thus, both the porous and the fluid layers simultaneously contribute to intermediate growth. This explains the growth characteristics with $\hat{d}$. For the slip parameter, increase signifies increased momentum transfer across the interface, thus establishing the dominance of the fluid layer in influencing the criticality. Increase in permeability (characterized by the Darcy number) assists relatively greater flow in the porous layer. Thus, with increase in permeability, the porous layer is able to influence the transient amplifications. Thus, the complex interactions among these parameters decide the short-time growth.

In further discussions, we consider oblique perturbations ($\alpha \neq 0, \quad \beta \neq 0$), and the effect of the parameters of the porous layer on the same. Figure 10 describes the effect of viscoplasticity, in terms of contours of maximum growth in the plane of streamwise and spanwise perturbations. At $Bn = 0.01$, the maximum growth is achieved by a spanwise perturbation. As the perturbations become oblique, the maximum growth is reduced. It is observed from figure 10(*a*) that the disturbance is streamwise at lower values of optimal, whereas it turns into a spanwise disturbance at the highest value of G_{max}. This is in conformity with earlier studies highlighting the role of spanwise disturbances in amplifying growth (Liu & Liu 2014; Liu *et al.* 2018). Nouar *et al.* (2007) also constructed contours of G_{max} for plane Bingham–Poiseuille flow. Their results are also presented in figure 10(*a*), for the sake of comparison. It is observed from figure 10(*a*) that, for a particular combination of (α, β), the G_{max}

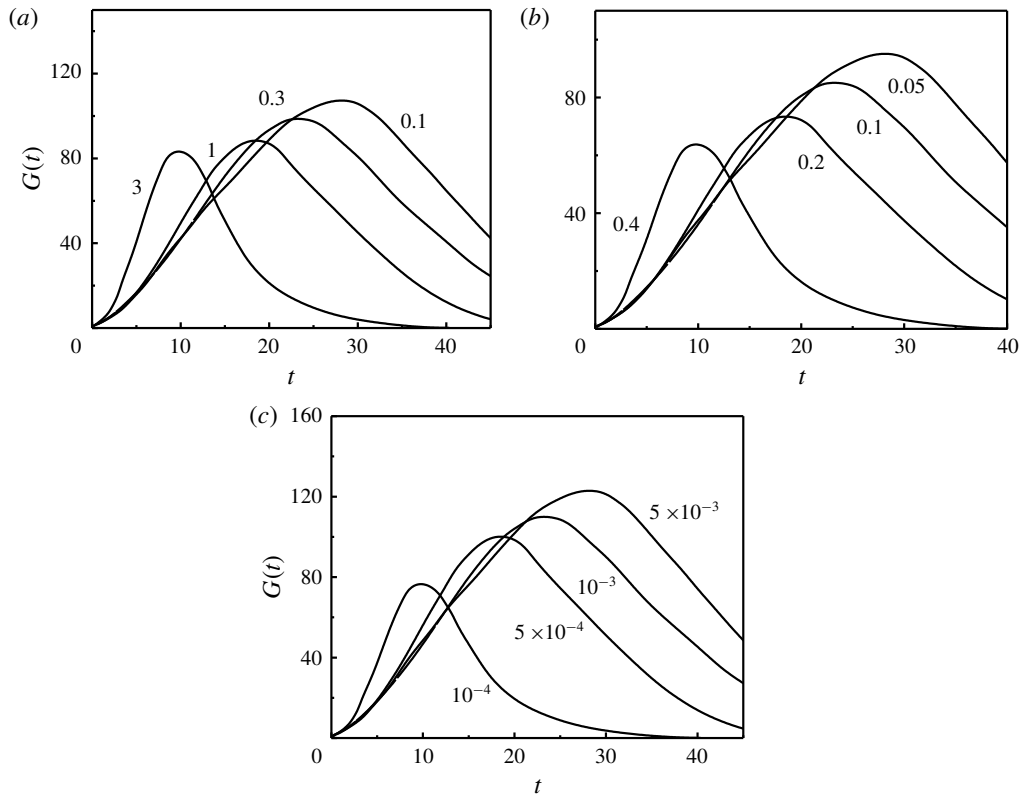

FIGURE 9. Growth rate curves depicting the effects of: (*a*) depth ratio $\hat{d}$; (*b*) slip parameter α_{BJ}; and (*c*) Darcy number δ. The numbers in the panels denote the respective values of the parameters. Here $Re = 600$ and $\beta = 4$ in all cases.

values obtained in the current study are higher than those of Nouar *et al.* (2007). This is because of the dominant role played by the porous layer in the present study for low Bn, as demonstrated in figure 7. Figure 10(*b*) depicts the contours of G_{max} for $Bn = 0.1$. A decrease in G_{max} with Bn is observed, for the same combination of (α, β). The decrease in maximum growth with increased viscoplasticity is due to the enhanced viscous dissipation. From figure 10(*a*,*b*), it is found that the magnitude of optimal growth reduces with Bn. Thus, although there is asymptotic long-time decay, viscoplasticity plays a stabilizing role in amplifying the short-time growth.

Figures 11–13 depict the effects of Darcy number, depth ratio and slip parameter with regards to the oblique perturbations. In figure 11, with increase in permeability, the optimal perturbation is increased. It increases from 150 to 290 as the permeability increases from $\delta = 5 \times 10^{-4}$ to 5×10^{-3}. This again demonstrates the destabilizing role played by permeability in creating short-time amplifications. The reason for this is the increased momentum in the porous layer with permeability. Also, as the perturbations turn from spanwise to oblique to streamwise, the maximum growth is lowered. However, at higher permeability, the perturbation producing maximum growth is oblique, although the streamwise component is negligible compared to the spanwise component.

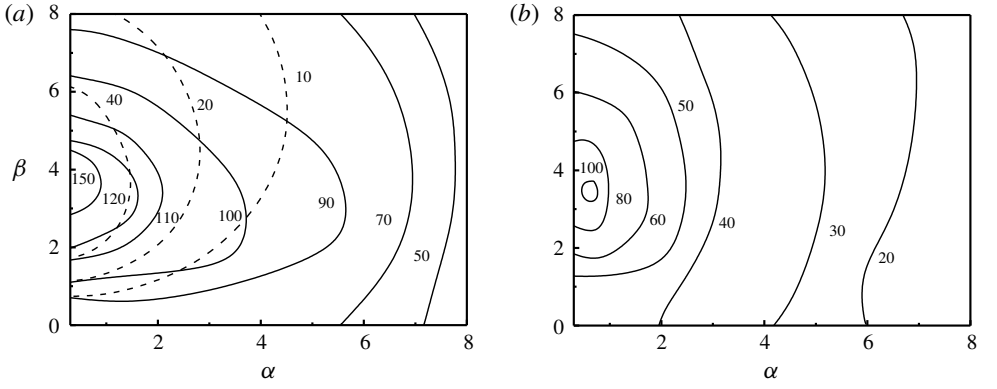

FIGURE 10. Effect of Bingham number: contours of G_{max} at (*a*) $Bn = 0.02$ and (*b*) $Bn = 0.1$. In (*a*), dashed lines refer to the studies of Nouar *et al.* (2007).

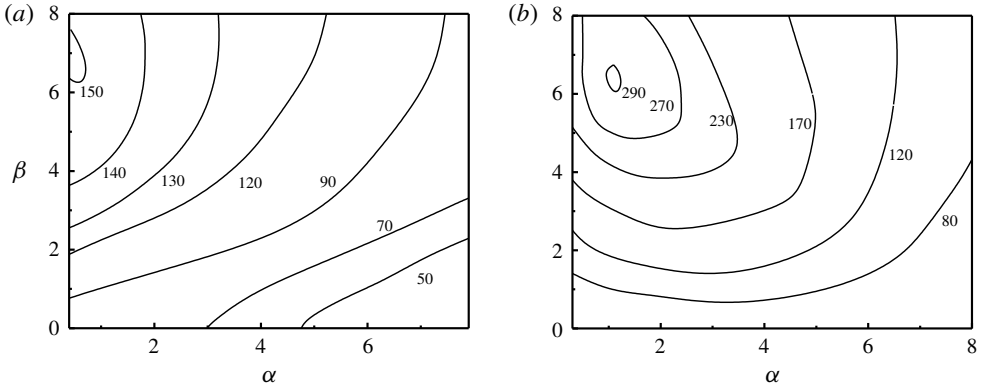

FIGURE 11. Effect of Darcy number: contours of G_{max} at (*a*) $\delta = 5 \times 10^{-4}$ and (*b*) $\delta = 5 \times 10^{-3}$.

Figure 12 expresses the effect of depth ratio. It is observed that the maximum growth is reduced with the increase in fluid layer thickness. Thus, as the relative influence of the fluid layer compared to the porous layer is increased in the flow system, there is a reduction in transient amplifications. The fluid modes restrict the growth of amplifications, leading to the reduction in the magnitudes of G_{max}. At very low depth ratio, the fluid layer has a small thickness, and a large part of the momentum is influenced by the porous layer. This explains the trend of the maximum growth with depth ratio. A similar behaviour is depicted by slip parameter in figure 13. At lower slip coefficient, the maximum growth perturbation is spanwise in nature. However, as the slip coefficient is increased, the perturbation becomes oblique.

3.5. *Mechanism of transient growth*

The shape of the optimal perturbation is explored in detail in figure 14. Figure 14(*a*) shows the shape of the optimal perturbation for $Bn = 0.02$ and $\hat{d} = 0.3$. It is observed that the perturbation is spanwise. Moreover, the optimal perturbations also protrude

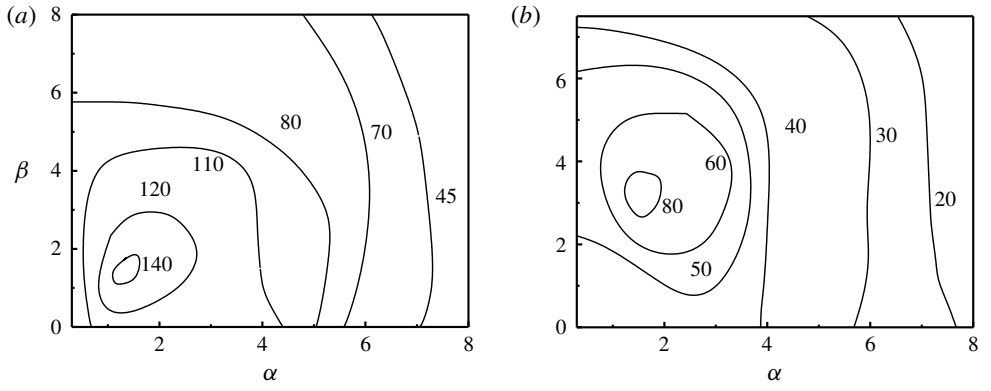

FIGURE 12. Effect of depth ratio: contours of G_{max} at (*a*) $\hat{d}=0.3$ and (*b*) $\hat{d}=3$.

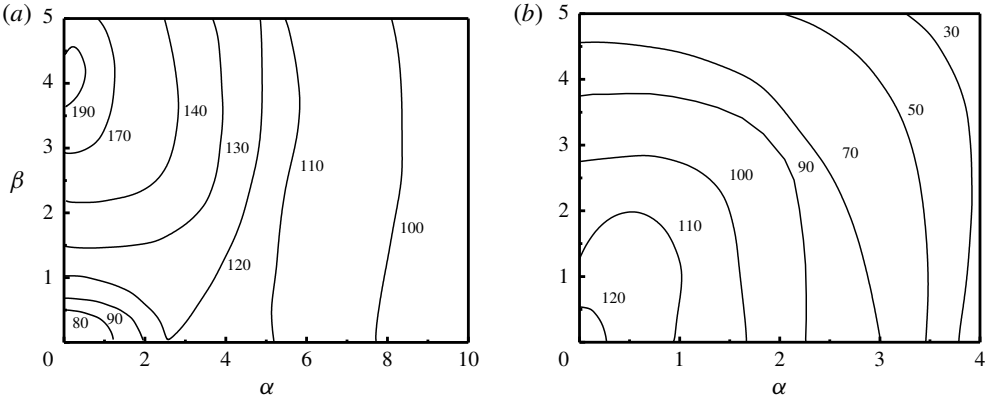

FIGURE 13. Effect of slip parameter: contours of G_{max} at (*a*) $\alpha_{BJ}=0.05$ and (*b*) $\alpha_{BJ}=0.2$.

into the porous layer. This explains the significance of the porous layer in deciding the flow transition characteristics, as also revealed in figure 7. Figure 14(*b*,*c*) displays the optimal perturbations for a high value of depth ratio ($\hat{d}=3$) for two different Bingham numbers, $Bn=0.02$ and 0.3. From the plots, it is observed that, at lower Bn, the optimal perturbation consists of spanwise streaks. However, it becomes oblique with larger Bn. This obliqueness of the optimal perturbation is possibly because of the fact that the effective viscosity of the Bingham fluid varies in a nonlinear fashion across the width of the channel. Moreover, at higher depth ratio, there is no protrusion of the optimal perturbation into the porous layer. The perturbations are confined to the fluid layer alone. This explains the relative significance of the fluid and the porous layers at high depth ratio.

It is worth while to discuss the mechanism of transient growth occurring here. In the case of inviscid shear flow, the streamwise component of the velocity perturbation has been found to grow linearly with time (Ellingsen & Palm 1975). This mechanism is commonly referred to as 'lift-up' (Reddy & Henningson 1993; Trefethen *et al.* 1993). However, for viscous shear flows, viscous dissipation plays an important role. In this case, there is initial linear growth of the streamwise velocity with time due to lift-up, and consequent damping due to viscosity (Butler & Farrell 1992; Farrell & Ioannou

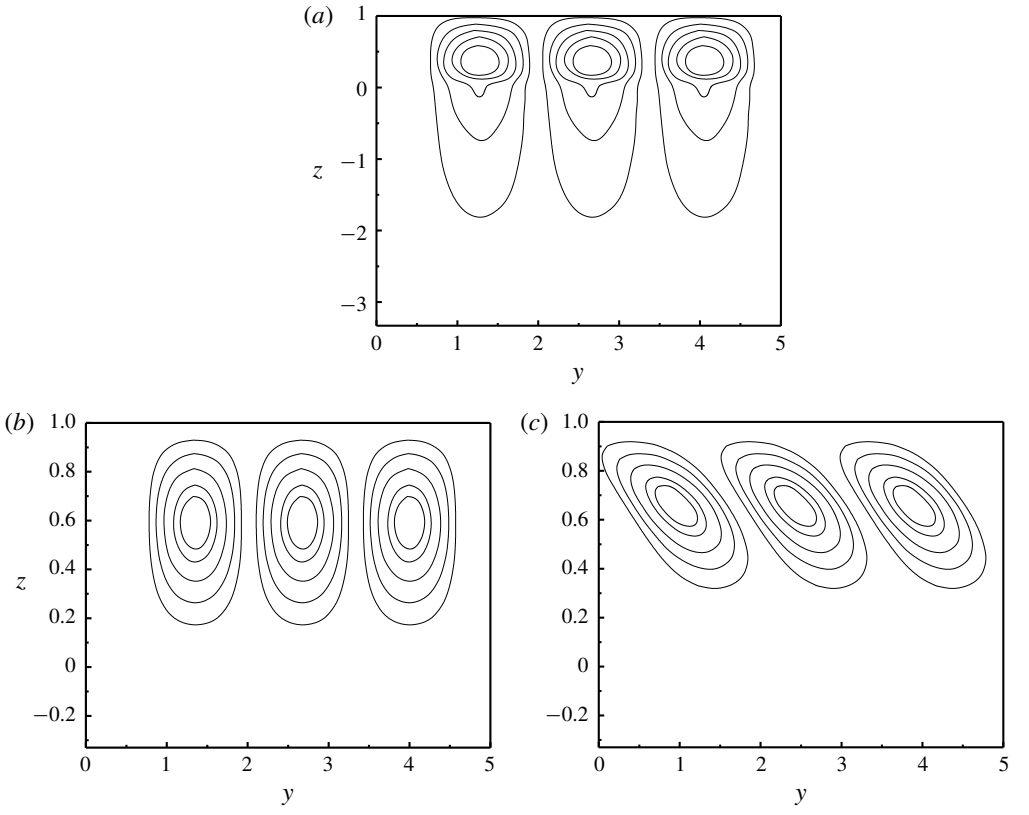

FIGURE 14. Optimal perturbation at $x=0$, $Re=600$ for: (*a*) $\hat{d}=0.3$, $Bn=0.02$; (*b*) $\hat{d}=3$, $Bn=0.02$; and (*c*) $\hat{d}=3$, $Bn=0.3$. Contour levels from outer to inner denote the values of u in the following order [0.1, 0.3, 0.5, 0.7, 0.9].

1993; Trefethen *et al.* 1993). The interplay of lift-up and Orr mechanisms contributes to transient growth of the oblique disturbances (Farrell & Ioannou 1993). They both act simultaneously, and the interaction between the two leads to the development of the transient growth. In our analysis, in the case of lower *Bn*, the shape of the optimal disturbance is found to be similar to that reported by Reddy & Henningson (1993) in the case of plane Newtonian–Poiseuille flow. It is known that the lift-up mechanism dominates transient growth in the case of such perturbations. However, at higher *Bn*, the perturbation becomes oblique in shape. As discussed, when the perturbation is oblique, both lift-up and Orr mechanisms become comparable. Thus, it may be said that transient growth is dominated by lift-up at lower *Bn*, while both lift-up and Orr mechanisms contribute to transient response at higher *Bn*.

3.6. *Description of the fluid–porous interface and the porous layer*

As may be observed from the expressions of the velocity profiles, there is a discontinuity in the axial velocity profile at the interface between the fluid and the porous layers. This discontinuity arises because of the Beavers–Joseph boundary condition, which is generally obtained from experimental study, and thus backed by experimental verification. The authors acknowledge the existence of more refined

interface conditions that have been proposed in recent times, for example, the ones by Ochoa-Tapia & Whitaker (1995*a*,*b*) and Bars & Worster (2006). However, each of these interface conditions also carries its own set of limitations. For example, the validity of the Bars–Worster boundary condition is questionable in the case of a sharp fluid–porous interface (Bars & Worster 2006). In addition, some of these conditions, like the boundary condition by Ochoa-Tapia & Whitaker, are generally used together with the Brinkman model. The limitations of the Brinkman model with regard to the current study have already been discussed in § 2.1. Taking all these factors into consideration, the current study uses the Beavers–Joseph condition to model the fluid–porous interface. The same has been adopted by other researchers as well (Chang *et al.* 2006; Deepu *et al.* 2015, 2016; Chang *et al.* 2017).

It may be mentioned that the Forchheimer model is not considered in the current analysis. Incorporation of the Forchheimer model ensures that the inertial effects are taken care of (Lyubimova *et al.* 2016). The Forchheimer model is generally considered when the Reynolds number in the porous layer (Re_m) is high. However, in the present study, Re_m in the porous layer is less than Re by approximately four orders of magnitude. This can be easily checked from the relation (2.47) between Re and Re_m. By taking representative values of the parameters ($Bn = 0.2$, $\beta_0 = 0.016$, $\hat{d} = 0.3$, $\alpha_{BJ} = 0.2$, $\delta = 0.001$, $A_{inh} = 2$), $Re/Re_m = 1.29 \times 10^4$. Therefore, Re_m is significantly small even for a seemingly high Re. Thus, there is negligible inertial effect in the porous layer. This is the primary reason behind neglecting inertial effects by a majority of researchers (Chang *et al.* 2006; Hill & Straughan 2008, 2009; Deepu *et al.* 2015, 2016; Chang *et al.* 2017).

4. Conclusion

The current study provides interesting insights into flow transition for Bingham fluids overlying an anisotropic and inhomogeneous porous layer. A linear stability analysis subject to infinitesimal perturbations shows the existence of fluid layer and porous layer modes, and the interplay between them in deciding the dominant mode of instability. Plots of critical energy Reynolds number versus the wavenumber are constructed to comprehend the conditions for no energy growth. The effects of permeability of the porous medium (in terms of Darcy number), the depth ratio (relative thicknesses of the fluid and porous layers), the slip coefficient and the yield stress (in terms of Bingham number) on criticality are assessed. The effect of anisotropy in the porous medium is found to be stabilizing. On the other hand, the inhomogeneity of the medium lowers the critical point, and is thus destabilizing in nature. The optimal perturbations are found to be spanwise at lower Bn, while they become oblique at higher Bn. It is observed that the lift-up mechanism dominates the transient growth at lower Bn, while at higher Bn, both lift-up and Orr mechanisms contribute to transient amplifications. It is envisaged that the present analysis would help in having a fundamental understanding of flow stability involving viscoplastic fluids in a porous channel configuration. In addition, it would also consequently lead to better designing of flow equipment involving viscoplastic fluid flow.

REFERENCES

ASSOCIATION OF SWISS ROAD AND TRAFFIC ENGINEERS 1999 *Characteristic Coefficients of Soils*. Swiss Standard SN 670 010b.

AURIAULT, J. L. 2009 On the domain of validity of Brinkman's equation. *Trans. Porous Med.* **79**, 215–223.

BALHOFF, M. T. & THOMPSON, K. E. 2004 Modeling the steady flow of yield-stress fluids in packed beds. *AIChE J.* **50**, 3034–3048.

BALMFORTH, N. J., FRIGAARD, I. A. & OVARLEZ, G. 2014 Yielding to stress: recent developments in viscoplastic fluid mechanics. *Annu. Rev. Fluid Mech.* **46**, 121–146.

BARS, M. L. & WORSTER, M. G. 2006 Interfacial conditions between a pure fluid and a porous medium: implications for binary alloy solidification. *J. Fluid Mech.* **550**, 149–173.

BEAVERS, G. S. & JOSEPH, D. D. 1967 Boundary conditions at a naturally permeable wall. *J. Fluid Mech.* **30**, 197–207.

BENTRAD, H., ESMAEL, A., NOUAR, C., LEFEVRE, A. & MESSAOUDENE, N. A. 2017 Energy growth in Hagen–Poiseuille flow of Herschel–Bulkley fluid. *J. Non-Newtonian Fluid Mech.* **241**, 43–59.

BIRD, R. B., DAI, G. C. & YARUSSO, B. J. 1983 Rheology and flow of viscoplastic materials. *Rev. Chem. Engng* **1**, 1–70.

BRINKMAN, H. C. 1949 A calculation of the viscous force exerted by a flowing fluid on a dense swarm of particles. *Appl. Sci. Res.* **1**, 27–34.

BUTLER, K. M. & FARRELL, B. F. 1992 Three-dimensional optimal perturbations in viscous shear flow. *Phys. Fluids* A **4**, 1637–1650.

CATON, F. 2006 Linear stability of circular Couette flow of inelastic viscoplastic fluids. *J. Non-Newtonian Fluid Mech.* **134**, 148–154.

CHANG, M. H., CHEN, F. & STRAUGHAN, B. 2006 Instability of Poiseuille flow in a fluid overlying a porous layer. *J. Fluid Mech.* **564**, 287–303.

CHANG, T. Y., CHEN, F. & CHANG, M. H. 2017 Stability of plane Poiseuille–Couette flow in a fluid layer overlying a porous layer. *J. Fluid Mech.* **826**, 376–395.

CHHABRA, R. P. & RICHARDSON, J. F. 1999 *Non-Newtonian Flow in the Process Industries – Fundamentals and Engineering Applications*. Butterworth Heinemann.

CHEN, F. & HSU, L. H. 1991 Onset of thermal convection in an anisotropic and inhomogeneous porous layer underlying a fluid layer. *J. Appl. Phys.* **69**, 6289.

CHEN, Y. L. & ZHU, K. Q. 2008 Couette–Poiseuille flow of Bingham fluids between two porous parallel plates with slip conditions. *J. Non-Newtonian Fluid Mech.* **153**, 1–11.

DAS, B. M. 2013 *Advanced Soil Mechanics*, 4th edn. CRC Press.

DASH, R. K., MEHTA, K. N. & JAYARAMAN, G. 1996 Casson fluid flow in a pipe filled with a homogeneous porous medium. *Intl J. Engng Sci.* **34**, 1145–1156.

DEEPU, P., ANAND, P. & BASU, S. 2015 Stability of Poiseuille flow in a fluid overlying an anisotropic and inhomogeneous porous layer. *Phys. Rev.* E **92**, 23009.

DEEPU, P., KALLURKAR, S., ANAND, P. & BASU, S. 2016 Stability of a liquid film flowing down an inclined anisotropic and inhomogeneous porous layer: an analytical description. *J. Fluid Mech.* **807**, 135–154.

DRAZIN, P. G. & REIID, W. H. 2004 *Hydrodynamic Stability*, 2nd edn. Cambridge University Press.

DURLOFSKY, L. & BRADY, J. F. 1987 Analysis of the Brinkman equation as a model for flow in porous media. *Phys. Fluids* **30**, 3329–3341.

ELLINGSEN, T. & PALM, E. 1975 Stability of linear flow. *Phys. Fluids* **18**, 487–488.

FARRELL, B. F. & IOANNOU, P. J. 1993 Optimal excitation of three-dimensional perturbations in viscous constant shear flow. *Phys. Fluids* A **5**, 1390–1400.

FRIGAARD, I. A. 2001 Super-stable parallel flows of multiple visco-plastic fluids. *J. Non-Newtonian Fluid Mech.* **100**, 49–75.

FRIGAARD, I. A., HOWISON, S. D. & SOBEY, I. J. 1994 On the stability of Poiseuille flow of a Bingham fluid. *J. Fluid Mech.* **263**, 133–150.

FRIGAARD, I. & NOUAR, C. 2003 On three-dimensional linear stability of Poiseuille flow of Bingham fluids. *Phys. Fluids* **15**, 2843.

HENNINGSON, D. S., LUNDBLADH, A. & JOHANSSON, A. V. 1993 A mechanism for bypass transition from localized disturbances in wall-bounded shear flows. *J. Fluid Mech.* **250**, 169–207.

HERZIG, J. P., LECLERC, D. M. & GOFF, P. L. 1970 Flow of suspensions through porous media – application to deep filtration. *Ind. Engng Chem.* **62**, 8–35.

HILL, A. A. & STRAUGHAN, B. 2008 Poiseuille flow in a fluid overlying a porous medium. *J. Fluid Mech.* **603**, 137–149.

HILL, A. A. & STRAUGHAN, B. 2009 Poiseuille flow in a fluid overlying a highly porous material. *Adv. Water Resour.* **32**, 1609–1614.

KABOUYA, N. & NOUAR, C. 2003 On the stability of a Bingham fluid flow in an annular channel. *C. R. Méc.* **331**, 149–156.

LANDRY, M. P., FRIGAARD, I. A. & MARTINEZ, D. M. 2006 Stability and instability of Taylor–Couette flows of a Bingham fluid. *J. Fluid Mech.* **560**, 321–353.

LIU, R., DING, Z. & HU, K. X. 2018 Stabilities in plane Poiseuille flow of Herschel–Bulkley fluid. *J. Non-Newtonian Fluid Mech.* **251**, 132–144.

LIU, R. & LIU, Q. 2009 Instabilities of a liquid film flowing down an inclined porous plane. *Phys. Rev.* E **80**, 036316.

LIU, R. & LIU, Q. S. 2014 Non-modal stability in Hagen–Poiseuille flow of a Bingham fluid. *Phys. Fluids* **26**, 14102.

LYUBIMOVA, T. P., LYUBIMOV, D. V., BAYDINA, D. T., KOLCHANOVA, E. A. & TSIBERKIN, K. B. 2016 Instability of plane-parallel flow of incompressible liquid over a saturated porous medium. *Phys. Rev.* E **94**, 013104.

MADANI, A., MARTINEZ, D. M., OLSON, J. A. & FRIGAARD, I. A. 2013 The stability of spiral Poiseuille flows of Newtonian and Bingham fluids in an annular gap. *J. Non-Newtonian Fluid Mech.* **193**, 3–10.

MALASHETTY, M. S. & MAHANTESH, S. 2010 The onset of convection in a binary fluid saturated anisotropic porous layer. *Intl J. Therm. Sci.* **49**, 867–878.

MANDAL, A. & BERA, A. 2015 Modeling of flow of oil-in-water emulsions through porous media. *Petrol. Sci.* **12**, 273–281.

MÉTIVIER, C., FRIGAARD, I. A. & NOUAR, C. 2009 Nonlinear stability of the Bingham Rayleigh–Bénard Poiseuille flow. *J. Non-Newtonian Fluid Mech.* **158**, 127–131.

MÉTIVIER, C. & MAGNIN, A. 2011 The effect of wall slip on the stability of the Rayleigh–Bénard Poiseuille flow of viscoplastic fluids. *J. Non-Newtonian Fluid Mech.* **166**, 839–846.

MÉTIVIER, C., NOUAR, C. & BRANCHER, J. P. 2005 Linear stability involving the Bingham model when the yield stress approaches zero. *Phys. Fluids* **17**, 104106.

MÉTIVIER, C. & NOUAR, C. 2008 On linear stability of Rayleigh–Bénard Poiseuille flow of viscoplastic fluids. *Phys. Fluids* **20**, 104101.

MÉTIVIER, C. & NOUAR, C. 2009 Linear stability of the Rayleigh–Bénard Poiseuille flow for thermodependent viscoplastic fluids. *J. Non-Newtonian Fluid Mech.* **163**, 1–8.

MÉTIVIER, C. & NOUAR, C. 2011 Stability of a Rayleigh–Bénard Poiseuille flow for yield stress fluids – comparison between Bingham and regularized models. *Intl J. Non-Linear Mech.* **46**, 1205–1212.

MÉTIVIER, C., NOUAR, C. & BRANCHER, J. P. 2010 Weakly nonlinear dynamics of thermoconvective instability involving viscoplastic fluids. *J. Fluid Mech.* **660**, 316–353.

MOYERS-GONZALEZ, M., BURGHELEA, T. I. & MAK, J. 2011 Linear stability analysis for plane-Poiseuille flow of an elastoviscoplastic fluid with internal microstructure for large Reynolds numbers. *J. Non-Newtonian Fluid Mech.* **166**, 515–531.

MOYERS-GONZALEZ, M. A., FRIGAARD, I. A. & NOUAR, C. 2004 Nonlinear stability of a visco-plastically lubricated viscous shear flow. *J. Fluid Mech.* **506**, 117–146.

NASH, S. & REES, D. A. S. 2017 The effect of microstructure on models for the flow of a Bingham fluid in porous media: one-dimensional flows. *Trans. Porous Med.* **116**, 1073–1092.

NIELD, D. A. & BEJAN, A. 2006 *Convection in Porous Media*. Springer.

NOUAR, C. & BOTTARO, A. 2010 Stability of the flow of a Bingham fluid in a channel: eigenvalue sensitivity, minimal defects and scaling laws of transition. *J. Fluid Mech.* **642**, 349–372.

NOUAR, C. & FRIGAARD, I. A. 2001 Nonlinear stability of Poiseuille flow of a Bingham fluid: theoretical results and comparison with phenomenological criteria. *J. Non-Newtonian Fluid Mech.* **100**, 127–149.

NOUAR, C., KABOUYA, N., DUSEK, J. & MAMOU, M. 2007 Modal and non-modal linear stability of the plane Bingham–Poiseuille flow. *J. Fluid Mech.* **577**, 211–239.

OCHOA-TAPIA, J. A. & WHITAKER, S. 1995*a* Momentum transfer at the boundary between a porous medium and a homogeneous fluid – I. Theoretical development. *Intl J. Heat Mass Transfer* **38**, 2635–2646.

OCHOA-TAPIA, J. A. & WHITAKER, S. 1995*b* Momentum transfer at the boundary between a porous medium and a homogeneous fluid – II. Comparison with experiment. *Intl J. Heat Mass Transfer* **38**, 2647–2655.

PAVLOV, K. B., ROMANOV, A. S. & SIMKHOVICH, S. L. 1974 Hydrodynamic stability of Poiseuille flow of a viscoplastic non-Newtonian fluid. *Fluid Dyn.* **9**, 996–998.

PAVLOV, K. B., ROMANOV, A. S. & SIMKHOVICH, S. L. 1975 Stability of Poiseuille flow of a viscoplastic fluid with respect to perturbations of finite amplitude. *Fluid Dyn.* **10**, 841–844.

PENG, J. & ZHU, K. Q. 2004 Linear stability of Bingham fluids in spiral Couette flow. *J. Fluid Mech.* **512**, 21–45.

PINARBASI, A. & LIAKOPOULOS, A. 1995 Stability of two-layer Poiseuille flow of Carreau–Yasuda and Bingham-like fluids. *J. Non-Newtonian Fluid Mech.* **57**, 227–241.

REDDY, S. C. & HENNINGSON, D. S. 1993 Energy growth in viscous channel flows. *J. Fluid Mech.* **252**, 209–238.

REES, D. A. S. 2015 Convection of a Bingham fluid in a porous medium. In *Handbook of Porous Media*, 3rd edn. (ed. K. Vafai), vol. 17, pp. 559–595. CRC Press.

SAHU, K. C. & MATAR, O. K. 2010 Three-dimensional linear instability in pressure-driven two-layer channel flow of a Newtonian and a Herschel–Bulkley fluid. *Phys. Fluids* **22**, 112103.

SAHU, K. C., VALLURI, P., SPELT, P. D. M. & MATAR, O. K. 2007 Linear instability of pressure-driven channel flow of a Newtonian and a Herschel–Bulkley fluid. *Phys. Fluids* **19**, 122101.

SCHMID, P. J. & HENNINGSON, D. S. 1992 A new mechanism for rapid transition involving a pair of oblique waves. *Phys. Fluids* A **4**, 1986–1989.

SCHMID, P. J. & HENNINGSON, D. S. 2001 *Stability and Transition in Shear Flows*. Springer.

SENGUPTA, S. & DE, S. 2019 Couette–Poiseuille flow of a Bingham fluid through a channel overlying a porous layer. *J. Non-Newtonian Fluid Mech.* **265**, 28–40.

SOLEIMANI, M. & SADEGHY, K. 2010 Dean instability of Bingham fluids in tangential flow between two fixed concentric cylinders. *J. Soc. Rheol. Japan* **38**, 125–132.

SOLEIMANI, M. & SADEGHY, K. 2011 Instability of Bingham fluids in Taylor–Dean flow between two concentric cylinders at arbitrary gap spacings. *Intl J. Non-Linear Mech.* **46**, 931–937.

SQUIRE, H. B. 1933 On the stability for three-dimensional disturbances of viscous fluid flow between parallel walls. *Proc. R. Soc. Lond.* A **142**, 621–628.

STRAUGHAN, B. & WALKER, D. W. 1996 Anisotropic porous penetrative convection. *Proc. R. Soc. Lond.* A **452**, 97–115.

TREFETHEN, L. N. & EMBREE, M. 2005 *Spectra and Pseudospectra: The Behavior of Nonnormal Matrices and Operators*. Princeton University Press.

TREFETHEN, L. N., TREFETHEN, A. E., REDDY, S. C. & DRISCOLL, T. A. 1993 Hydrodynamic stability without eigenvalues. *Science* **261**, 578–584.

TRIPATHI, D., YADAV, A., BEG, O. A. & KUMAR, R. 2018 Study of microvascular non-Newtonian blood flow modulated by electroosmosis. *Microvasc. Res.* **117**, 28–36.